Liquid and liquid-gas flows at all speeds: Reference solutions and numerical schemes

Sebastien Lemartelot, Boniface Nkonga, Richard Saurel

Liquid and liquid-gas flows at all speeds : Reference solutions and numerical schemes

S. LeMartelot , B. Nkonga , R. Saurel

RESEARCH REPORT
N° 7935
Avril 2012
Project-Teams SMASH et PUMAS

ISSN 0249-6399 ISRN INRIA/RR--7935--FR+ENG

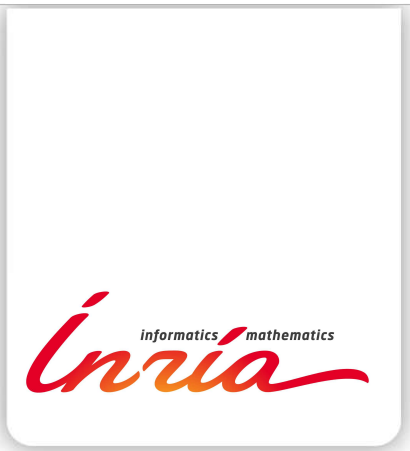

Liquid and liquid-gas flows at all speeds : Reference solutions and numerical schemes

S. LeMartelot *, B. Nkonga †, R. Saurel ‡

Project-Teams SMASH et PUMAS

Research Report n° 7935 — Avril 2012 — 61 pages

* Polytech'Marseille, Aix-Marseille University, UMR CNRS 6595 IUSTI, 5 rue E. Fermi, 13453 Marseille Cedex 13, France

† University of Nice, LJAD UMR CNRS 7351, Parc Valrose, 06108 Nice Cedex, INRIA Sophia-Antipolis

‡ Polytech'Marseille, Aix-Marseille University, UMR CNRS 6595 IUSTI, 5 rue E. Fermi, 13453 Marseille Cedex 13, France, INRIA Sophia-Antipolis

RESEARCH CENTRE
SOPHIA ANTIPOLIS – MÉDITERRANÉE

2004 route des Lucioles - BP 93
06902 Sophia Antipolis Cedex

Abstract: All speed flows and in particular low Mach number flow algorithms are addressed for the numerical approximation of the Kapila et al. [19] multiphase flow model. This model is valid for fluid mixtures evolving in mechanical equilibrium but out of temperature equilibrium and is efficient for material interfaces computation separating miscible and non-miscible fluids. In this context, the interface is considered as a numerically diffused zone, captured as well as all present waves (shocks, expansion waves). The same flow model can be used to solve cavitating and boiling flows [39]. Many applications occurring with liquid-gas interfaces and cavitating flows involve a very wide range of Mach number variations, from 10^{-3} to 100 with respect to the mixture sound speed. It is thus important to address numerical methods free of restrictions regarding the Mach number.
To assess the accuracy of such schemes, reference solutions are needed and there is a clear lack in this domain. We address here exact one-dimensional liquid and liquid-gas compressible flows solutions in nozzles. The exact solution is first derived for the compressible single liquid phase Euler equations and extends the well known ideal gas dynamic nozzle flow solutions. This reference solution is then extended to the Kapila et al. [19] model that contains two entropies and non conventional shock relations. The all Mach number scheme is then derived. A preconditioned Riemann solver is built and embedded into the Godunov explicit scheme. It is shown that this method converges to exact solutions but needs too small time steps to be efficient. An implicit version is then derived, in one dimension first and second in the frame of 3D unstructured meshes. Two-phase flow preconditioning is then addressed in the frame of the Saurel et al [38] algorithm. Modifications of the preconditioned Riemann solver are needed and detailed. Convergence of both single phase and two-phase numerical solutions are demonstrated with the help of exact ones. Last, the method is illustrated by the computation of real cavitating flows in Venturi nozzles. Vapor pocket size and instability frequencies are perfectly reproduced by the model and method without using any parameters. In particular, no turbulence model is used.

Key-words: hyperbolic systems, multifluid, multiphase, Venturi, cavitation, preconditioned, unstructured meshes, HLLC.

Liquid and liquid-gas flows at all speeds : Reference solutions and numerical schemes

Résumé :

Mots-clés :

1 Introduction

Liquid-gas mixtures and interfacial flows arise in many natural and industrial situations occurring in fluid mechanics, nuclear, environmental and chemical engineering. Most computational approaches consider the two fluids as incompressible (Hirt and Nichols [17], Lafaurie et al [22], Menard et al [24]) to cite a few. High Mach number flows with material interfaces have also been the subject of important efforts, with various approaches: Front Tracking [11], Level Set and Ghost Fluid [10], diffuse interfaces [1], [34], [38] and others. Only a few works deal with incompressible liquid and compressible gas [18]. However, in many applications gas compressibility is of paramount importance as, for example, when phase change occurs. In cavitating flows, compressibility of all phases is important as the liquid phase change occurs under liquid expansion effects. Moreover, when liquid-gas mixtures appear, the sound propagates with the mixture sound speed [45] that has a non monotonic behaviour with respect to the volume fraction, resulting in very low sound speed, of the order of a few meters per second. There is thus no difficulty to reach hypersonic flow conditions with liquid gas mixtures. Consequently, it is important to build numerical methods able to deal with incompressible flows, transonic flows and even hypersonic flows in the presence of wave dynamics. This issue has been addressed intensively in the context of single phase flows since Harlow and Amsden [15] extending incompressible flow solvers to compressible flows and Turkel [43] extending compressible flow solvers to the incompressible limit. For now, it seems that multiphase flows in the low Mach regime has been addressed more by methods issued of incompressible flows. However, this poses difficulties when wave dynamics is present, as incompressible flow solvers are not conservative in the compressible flow sense. Also, these methods have difficulties when large density ratios are present. At liquid gas interfaces, the density ratio may exceed several thousands.
In the present work we consider liquid-gas interfaces as diffuse numerical zones and adopt the Kapila et al. [19] model. This has some advantages:
- The interfaces are handled routinely, as any point of the flow.
- The dynamic appearance of interfaces (not present initially) is possible thanks to the volume fraction equation structure that allows volume fraction growth in zones where the velocity divergence is non zero. This occurs typically in expansion and compression waves and is of major importance in cavitating flows.
- The phases mass, mixture momentum and mixture energy are expressed under conservative form, insuring correct wave dynamics in pure fluids zones.
- The addition of surface tension [29] as well as phase transition [39] can be done quite easily in a thermodynamically consistent way. In other words, capillary effects are modeled with the help of a capillary tensor that enters in the momentum and energy fluxes conservatively. The entropy is also preserved. When phase transition is considered, the model guarantees mixture entropy production.
This approach has obviously some drawbacks:
- The interfaces can be excessively diffused, especially when dealing with long time evolutions. But this is exactly the same drawback as contact discontinuity smearing in gas dynamics computations. Efforts to reduce numerical diffusion have been done recently by Kokh and Lagoutière [21] and Shuckla et al. [41].
- Non-conservative equations are present and the numerical approximation of non-conservative terms poses difficulties in the presence of shocks [36], [30], [38], [32].
- The building of all Mach number method for this kind of hyperbolic flow model is not an easy task, as will be shown latter.
As the flow model is conservative regarding the phases mass equations, mixture momentum and mixture energy and since the system is hyperbolic we will follow a method issued from compress-

ible flow dynamics [43]. This choice is motivated by the importance of the pressure waves present in many applications, the presence of huge density ratios at interfaces, that are easier to handle with discontinuity capturing schemes and by the presence of huge Mach number variations. For specific applications, this is mandatory as for example with:
- liquid-gas flows in nozzle and Venturi tunnels,
- high performance turbopumps where cavitation appears,
- propellers,
- water waves breaking,
- flash vaporization.

The first difficulty with the design of a numerical scheme is related to its convergence. This poses the question of reference solutions. Most low Mach number methods predictions are compared against multidimensional flow solutions, typically around airfoils, under the assumption of potential flows. We believe it is simpler and more efficient to address one-dimensional flows. In this aim, liquid nozzle flow solution is determined in the context of the Euler equations and stiffened gas equation of state (SG EOS). This extends the well known ideal gas nozzle flow solutions. In the low Mach regime, the exact compressible solution is compared to the incompressible one, showing excellent agreement. This reference solution allows immediate comparison of conventional hyperbolic flow solvers in this limit. It is shown that conventional methods (Godunov type for example) result in several orders of magnitude errors in the pressure computation. We then address liquid-gas nozzle flow solution for the Kapila et al. [19] model, again for fluids governed by the SG EOS. The single phase exact solution is extended to the two-phase case with the help of multiphase shock relations [35]. Thanks to these reference solutions, we then address all Mach number schemes building in the frame of Turkel [43] formulation.

From theoretical standpoint, mathematical analysis of the low Mach number limit for classical solutions of the compressible Navier-Stokes has been investigated by many authors (Ebin [8] , Klainerman and Majda [20], Schochet [40], Metivier and Schochet [26], and many others). Alazard [2] proved, in a rigorous analysis and general context, the existence of uniformly bounded incompressible limit of the full Navier-Stokes equations. The existence time is there independent of the Mach, the Reynolds and the Peclet numbers and thereby includes the limit for the Euler equation as well. On this theoretical basis, we first consider the single phase Euler equations and derive an approximate preconditioned Riemann solver. When the Godunov scheme is used with this Riemann solver, convergence to the exact nozzle flow solution is obtained. However, the method requires too small time steps (much smaller that the conventional CFL restriction) to be stable. We thus consider implicit formulation to overcome this restriction. The HLLC flux of Toro et al. [42] is considered and a Taylor expansion is done to express its time variation. The method is first presented in the context of the one-dimensional Euler equations and then extended to the one-dimensional Kapila et al. [19] model. After validation against the exact one-dimensional two-phase nozzle flow solution, 3D extension of the algorithm for unstructured meshes is presented. Computational examples are shown in 3D. In particular, a real cavitating flow in 3D Venturi channel is examined. With the help of the new method, perfect agreement with the measured cavitation pocket size and detachment frequency is obtained without having recourse to any model or method parameter.

The paper is organized as follows. In Section 2 the various flow models under interest are presented: the Euler equations, the Kapila et al. [19] model, the pressure non-equilibrium model of Saurel et al. [38] that is used to solve the non-conservative pressure equilibrium model of Kapila et al. [19]. In Section 3, the exact liquid one-dimensional nozzle flow solution is detailed. It is then extented to two-phase liquid-gas flows. In Section 4 the low Mach single phase Riemann solver is presented. It uses the preconditioned Euler equations in the Riemann problem resolution only, while the conventional conservative formulation is used for the solution update. Its

extension to the two-phase flow model is then examined. To overcome the stability restriction of these methods, the implicit formulation of the Godunov method is given in 1D in the context of the Euler equations, with the HLLC Riemann solver and preconditioned formulation. Method convergence to the exact solution is demonstrated in both low and high Mach conditions. The two-phase flows extension on the basis of the pressure relaxation model of Saurel et al. [38] is then addressed, in one-dimension again. Convergence to the exact two-phase solution and three dimensional extension of the algorithm for multiphase flows are addressed in the same section. Computational example and validations against experimental data are given in section 5. Conclusions are given in Section 6.

2 Flow Models

In the present study, we are going to consider various flow models, single and two-phase. The single phase one correspond to the Euler equations:

$$\begin{aligned} &\frac{\partial \rho}{\partial t} + div\left(\rho \mathbf{u}\right) = 0 \\ &\frac{\partial \rho \mathbf{u}}{\partial t} + div\left(\rho \mathbf{u} \otimes \mathbf{u} + P\right) = 0 \\ &\frac{\partial \rho E}{\partial t} + div\left((\rho E + P)\mathbf{u}\right) = 0 \end{aligned} \tag{1}$$

where ρ is the density, $\mathbf{u}$ is the velocity vector, P is the pressure, E is the total energy, with $E = e + \frac{1}{2}\mathbf{u}^2$, whith e the internal energy. The thermodynamic closure is achieved by a convex EOS: $P = P(\rho, e)$. In the present work the SG EOS [14] [25] is used:

$$p = (\gamma - 1)\rho e - \gamma P_\infty \tag{2}$$

γ and P_∞ are parameters of the EOS, obtained from reference thermodynamic curves, characteristic of the material and transformation under study. See Le Metayer et al (2004) [27] for details.

The two phase flow model we will consider is the one of Kapila et al (2001) [19]. It describes multiphase mixtures evolving in mechanical equilibrium (equal pressures and equal velocities). It is particularly suited to materials interfaces computations, considered as numerical diffusion zones (see for example Saurel et al [38])

$$\begin{aligned} &\frac{\partial \alpha_1}{\partial t} + \mathbf{u} \bullet \mathbf{grad}\left(\alpha_1\right) = K div\left(\mathbf{u}\right) \\ &\frac{\partial \alpha_1 \rho_1}{\partial t} + div\left(\alpha_1 \rho_1 \mathbf{u}\right) = 0 \\ &\frac{\partial \alpha_2 \rho_2}{\partial t} + div\left(\alpha_2 \rho_2 \mathbf{u}\right) = 0 \qquad \text{where} \quad K = \frac{\rho_2 c_2^2 - \rho_1 c_1^2}{\frac{\rho_1 c_1^2}{\alpha_1} + \frac{\rho_2 c_2^2}{\alpha_2}} \\ &\frac{\partial \rho \mathbf{u}}{\partial t} + div\left(\rho \mathbf{u} \otimes \mathbf{u} + P\right) = 0 \\ &\frac{\partial \rho E}{\partial t} + div\left((\rho E + P)\mathbf{u}\right) = 0 \end{aligned} \tag{3}$$

c_k represents the sound speed defined by $c_k^2 = \frac{\partial p_k}{\partial \rho_k}\Big)_{s_k}, k = 1, 2,$
P represents the mixture pressure,
E represents mixture total energy,
α_k represent the phases volume fraction,
ρ_k represent the phase densities.

Model's thermodynamic closure is achieved with the help of the mixture energy definition:

$$\rho e = \alpha_1 \rho_1 e_1 + \alpha_2 \rho_2 e_2$$

and the pressure equilibrium condition: $p_1 = p_2$. In the context of fluids governed by the SG EOS (2), the mixture EOS reads:

$$P = \frac{\rho e - (\frac{\alpha_1 \gamma_1 P_{\infty,1}}{\gamma_1 - 1} + \frac{\alpha_2 \gamma_2 P_{\infty,2}}{\gamma_2 - 1})}{\frac{\alpha_1}{\gamma_1 - 1} + \frac{\alpha_2}{\gamma_2 - 1}} \tag{4}$$

The numerical approximation of the Kapila et al. [19] model is addressed in the frame of Godunov type finite volume schemes. These schemes are appropriate for non linear hyperbolic equations and proceed with a transport step achieved with the help of appropriate Riemann solvers and a projection step based on cell averages and thermodynamic computations. To overcome the difficulties related to the approximation of the non conservative term $Kdiv(u)$ in the volume fraction equation of System (3) a pressure non equilibrium system (5) is considered during the transport step and a proper projection is achieved to recover the target model (3). The pressure non equilibrium system reads:

$$\begin{aligned}
&\frac{\partial \alpha_1}{\partial t} + \mathbf{u} \bullet \mathbf{grad}\,(\alpha_1) = \mu(p_1 - p_2) \\
&\frac{\partial \alpha_1 \rho_1}{\partial t} + div\,(\alpha_1 \rho_1 \mathbf{u}) = 0 \\
&\frac{\partial \alpha_2 \rho_2}{\partial t} + div\,(\alpha_2 \rho_2 \mathbf{u}) = 0 \\
&\frac{\partial \alpha_1 \rho_1 e_1}{\partial t} + div\,(\alpha_1 \rho_1 e_1 \mathbf{u}) + \alpha_1 p_1 div\,(\mathbf{u}) = -p_I \mu(p_1 - p_2) \\
&\frac{\partial \alpha_2 \rho_2 e_2}{\partial t} + div\,(\alpha_2 \rho_2 e_2 \mathbf{u}) + \alpha_2 p_2 div\,(\mathbf{u}) = p_I \mu(p_1 - p_2) \\
&\frac{\partial \rho \mathbf{u}}{\partial t} + div\,(\rho \mathbf{u} \otimes \mathbf{u} + P) = 0 \\
&\frac{\partial \rho E}{\partial t} + div\,((\rho E + P)\mathbf{u}) = 0
\end{aligned} \tag{5}$$

Where
μ represents the pressure relaxation coefficient,
p_I represents the interfacial pressure defined by $p_I = \dfrac{Z_1 p_2 + Z_2 p_1}{Z_1 + Z_2}$,
with $Z_k = \rho_k c_k$, the phase k acoustic impedance.
e_k and p_k represent the phase k internal energy and pressure respectively.

It is important to note that in this system the internal energies of each phase are independent variables and their evolution is described by two additional equations. The mixture pressure is now related to the phases' internal energies:

$$P = \alpha_1 p_1 + \alpha_2 p_2 \tag{6}$$

where $p_1 = p_1(\rho_1, e_1)$ and $p_2 = p_2(\rho_2, e_2)$

The non equilibrium system (5) is hyperbolic and appropriate to overcome the difficulties related

to the discretisation of the volume fraction, in particular regarding positiveness issues. System (5) is used to reach solutions of System (3) in the limit of infinite pressure relaxation, i.e. when μ tends to infinity.
It is worth to mention that System (5) is overdetermined. Indeed, the total energy equation is a consequence of the phases energy equations and the mixture momentum one. This overdetermination will be used to correct the inacuracy appearing during the numerical integration of $\alpha_k p_k div(\mathbf{u})$, the non conservative terms of the internal energy equations [38]. Overdetermined systems have already been considered for numerical approximation issues in different contexts by Babii et al. [3] for example.
To be more precise, each integration time step is structured as follows [38]:

- **Initialization**: At a given time step, the flow is in mechanical equilibrium, in particular in pressure equilibrium. The set of variables is given by:

$$(\alpha_1^n, \rho_1^n, \rho_2^n, u^n, e_1^n(\rho_1^n, p^n), e_2^n(\rho_2^n, p^n), E^n)$$

- **Non equilibrium evolution**: The pressure relaxation terms are removed ($\mu = 0$) and the hyperbolic pressure non equilibrium system (5) is solved. At the end of this evolution step a temporary flow state is determined, out of pressure equilibrium:

$$(\tilde{\alpha}_1^{n+1}, \tilde{\rho}_1^{n+1}, \tilde{\rho}_2^{n+1}, \tilde{u}^{n+1}, \tilde{e}_1^{n+1}, \tilde{e}_2^{n+1}, \tilde{E}^{n+1})$$

- **Projection to pressure equilibrium**: This step deals with the projection of the previous pressure non equilibrium state onto a pressure equilibrium one:

$$(\alpha_1^{n+1}, \rho_1^{n+1}, \rho_2^{n+1}, u^{n+1}, e_1^{n+1}(\rho_1^{n+1}, p^{n+1}), e_2^{n+1}(\rho_2^{n+1}, p^{n+1}), E^{n+1})$$

This is done by determining the asymptotic solution of the remaining relaxation ODE system in the limit $\mu \to +\infty$.The asymptotic state is determined by the resolution of a non linear algebraic equation. Details may be found, for example, in [38].
It is worth to mention that:

- The equilibrium pressure p^{n+1} is determined from the mixture EOS (4), based on the mixture total energy E^{n+1}, for which there is no conservation issue.

- Both steps in this strategy preserves volume fraction positivity.

- Both steps preserve phases' mass conservation, mixture momentum and energy conservation.

- The entropy inequality is also preserved during each step.

This algorithm has shown robustness, accuracy and versatility for various flow models ranging from interfaces, supercavitating flows [39], detonation waves [31], powder compaction [37], solid-fluid coupling [9] in severe high speed conditions. We address here arbitrary velocity flow conditions and particularly low Mach number conditions.
The first issue in this frame is related to the determination of reference solutions to check method convergence and improve existing schemes in arbitrary flow conditions. This issue is addressed in the next section for single and two-phase steady flows in nozzles and Venturi ducts.

3 Reference solutions

The aim is to determine the one dimensional two phase nozzle flow solution of System (3) for fluids governed by the SG EOS (2). For the sake of simplicity in the presentation, we first detail the exact solution for single phase liquid flows governed by the Euler equations (System 1) and SG EOS (2). We then extend the solution method determination to the two-phase nozzle flow context.

3.1 Single phase nozzle flow

In this section, the single phase exact solution determination is addressed. To do so, we consider a nozzle connected to a tank at left and opened to the atmosphere at the right outlet, as shown in the Figure 1. The tank state is denoted by subscript "0" while the outlet state is denoted by

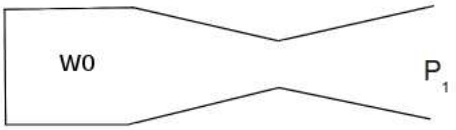

Figure 1: Nozzle connected to a tank at the inlet and to a prescribed pressure at the outlet

subscript "out". The tank state is defined by :

$$W_0 = \begin{pmatrix} \rho_0 \\ u_0 \\ p_0 \end{pmatrix}$$

Where ρ_0 and p_0 are prescribed density and pressure respectively and $u_0 = 0$. In order to determine the nozzle flow solution, it is first necessary to determine the flow configuration. It can be subsonic everywhere, supersonic in the divergent, supersonic with a shock in the divergent. All theses configurations have to be considered. To do so, various critical pressure ratios have to be determined.

3.1.1 Critical pressure ratios

The first critical pressure ratio corresponds to the appearance of a sonic state throath. Obviously, for liquids, such sonic state requires very high pressure ratios. But, as shown later, such state can be reached with moderate pressure ratios when dealing with two phase mixtures.

Critical pressure ratio 1 (cpr1) The critical pressure ratio, cpr1, is defined as the outlet/tank pressure ratio corresponding to a subsonic flow everywhere except at the throat where chocking conditions ($u = c$) appear.
As the flow is isentropic everywhere, the following relations are used:

$$H^* = H_0 \quad \text{and} \quad s^* = s_0 \tag{7}$$

Where:
s represents the entropy
H represents the total enthalpy, defined by $H = e + \dfrac{p}{\rho} + \dfrac{1}{2}u^2$
The "*" superscript represents the nozzle throat state for which $u^* = c^*$.

Using the SG EOS, relations (7) become:

$$\frac{\gamma\left(p^*+P_\infty\right)}{\left(\gamma-1\right)\rho^*}+\frac{1}{2}u^{*2}=H_0 \quad \text{and} \quad \frac{p^*+P_\infty}{\rho^{*\gamma}}=\frac{p_0+P_\infty}{\rho_0^\gamma} \tag{8}$$

The last unknown is the velocity at the nozzle throat, u^*.
The SG EOS sound speed reads :

$$c=\sqrt{\gamma\frac{p+P_\infty}{\rho}} \tag{9}$$

As, $u^*=c^*$, combining relation (8) and (9) yields the throat pressure, p^* :

$$p^*+P_\infty=(p_0+P_\infty)(\frac{\gamma+1}{2})^{\frac{\gamma-1}{\gamma}} \tag{10}$$

As the critical pressure, p^*, is known, the complete critical state W^* is determined with the help of relations (8).
It is necessary to determine the state in the outlet section. Relations (8) can be used again as :

$$\frac{\gamma\left(p_{out}+P_\infty\right)}{\left(\gamma-1\right)\rho_{out}}+\frac{1}{2}U_{out}=H_0 \quad \text{and} \quad \frac{p_{out}+P_\infty}{\rho_1^\gamma}=\frac{p_0+P_\infty}{\rho_0^\gamma} \tag{11}$$

The closure relation now corresponds to the mass conservation between the throat section and the outlet.

$$P_{out}=\rho_{out}U_{out}A_o=\rho^*u^*A^*=m^* \tag{12}$$

where A_o represents the outlet section area and A^* the nozzle throat section area.
Using equation (11), the density in the outlet section can be expressed as a function of p_{out} only. Thus, the following expression is obtained for the velocity in the outlet section U_{out}:

$$U_{out}=\frac{m^*}{\rho_{out}(p_{out})A_o} \quad \text{with} \quad \rho_{out}=\rho_0\left(\frac{p_{out}+P_\infty}{p_0+P_\infty}\right)^{\frac{1}{\gamma}} \tag{13}$$

Combining relations (13) and (11), a non-linear function of p_{out} is obtained:

$$\frac{\gamma\left(p_{out}+P_\infty\right)}{\left(\gamma-1\right)\rho_{out}(p_{out})}+\frac{1}{2}\left(\frac{m^*}{\rho_{out}(p_o)A_o}\right)^2-H^*=0 \tag{14}$$

This equation admits two roots : $p_{out}=p_{cpr1}$ and $p_{out}=p_{cpr3}$.
The subsonic branch corresponds to the pressure ratio cpr1. To determine it, the Newton method is used with initial guess for the outlet pressure $p_{out}=p^*$. Then, cpr1 is defined as $cpr1=\frac{p_{cpr1}+P_\infty}{p_0+P_\infty}$.

Critical pressure ratio 3 (cpr3) This solution corresponds to the supersonic branch of equation (14). Is is obtained again from (14) with the Newton method by taking the initial pressure guess $p_{out}=(1+10^{-6})P_\infty$. When convergence is reached, the outlet pressure is determined as $p_{out}=p_{cpr3}$. The critical pressure ratio cpr3 is obtained as $cpr3=\frac{p_{cpr3}+P_\infty}{p_0+P_\infty}$.

Critical pressure ratio 2 (cpr2) The critical pressure ratio, cpr2, corresponds to a supersonic flow in the nozzle divergent except at the outlet section where a steady shock is present.
The flow entering the shock has precisely the state corresponding to W_{cpr3}. The shocked state is obtained with the help of the Rankine-Hugoniot relations :

$$(\rho u)_{cpr3} = (\rho u)_{cpr2} \tag{15}$$

$$\left(\rho u^2 + p\right)_{cpr3} = \left(\rho u^2 + p\right)_{cpr2} \tag{16}$$

$$e_{cpr2} - e_{cpr3} + \frac{p_{cpr2} + p_{cpr3}}{2}\left(v_{cpr2} - v_{cpr3}\right) = 0 \tag{17}$$

With the help of the SG EOS , Equation (17) becomes:

$$\frac{v_{cpr2}}{v_{cpr3}} = \mathcal{Q}\left(p_{cpr2}, p_{cpr3}\right) = \frac{(\gamma-1)(p_{cpr2}+P_\infty) + (\gamma+1)(p_{cpr3}+P_\infty)}{(\gamma-1)(p_{cpr3}+P_\infty) + (\gamma+1)(p_{cpr2}+P_\infty)} \tag{18}$$

where v represents the specific volume, $v = \dfrac{1}{\rho}$.
Combining relations (18), (15) and (16), a non-linear function of p_{cpr2} is obtained:

$$p_{cpr3} - p_{cpr2} + \rho_{cpr3}\left(u_{c3}\right)^2\left(1 - \mathcal{Q}\left(p_{cpr2}, p_{cpr3}\right)\right) = 0 \tag{19}$$

Again, the Newton method is used to determine p_{cpr2}.
The initial pressure guess in the Newton method is $p_{cpr2} = p_{cpr1}$, as $p_{cpr1} > p_{cpr2} > p_{cpr3}$.

3.1.2 Derivation of the Nozzle flow profile : Single phase Isentropic

When the pressure ration $PR = \dfrac{p_{out} + P_\infty}{p_0 + P_\infty}$ is either greater than cpr1 or lower than cpr2, the flow is isentropic all over the nozzle. As the outlet pressure is given, we can computed the remaining variables at this section. Indeed, the second relation of (8) expressed between the tank and the outlet gives the outlet density :

$$\rho_{out} = \rho_0\left(\frac{p_{out} + P_\infty}{p_0 + P_\infty}\right)^{\frac{1}{\gamma}} \tag{20}$$

The outlet velocity is obtained from the first relation in equation (8) appied to the outlet section:

$$U_{out} = \sqrt{2\left[H_0 - \frac{\gamma(p_{out} + P_\infty)}{(\gamma-1)\rho_{out}}\right]} \tag{21}$$

Then, from the variables computed at the outlet and relations (8) expressed for any cross section A_i, we obtained

$$\frac{\gamma(p_i + P_\infty)}{(\gamma-1)\rho_i} + \frac{1}{2}u_i^2 = H_0, \tag{22}$$

$$\frac{p_i + P_\infty}{\rho_i^\gamma} = \frac{p_0 + P_\infty}{\rho_0^\gamma}. \tag{23}$$

The system is closed by the mass conservation relation expressed between the outlet section and the one of interest :

$$\rho_i u_i A_i = m^* \tag{24}$$

Combining previous relations, we obtained a non-linear function defining the pressure p_i at any section:

$$\frac{\gamma\left(p_i + P_\infty\right)}{\left(\gamma - 1\right)\rho_i(p_i)} + \frac{1}{2}\left(\frac{m^*}{\rho_i(p_i)A_i}\right)^2 - H_0 = 0 \tag{25}$$

It is solved again with the Newton method. Once the pressure p_i is determined, the density ρ_i and the velocity u_i are determined from (23) and (24) respectively.

3.1.3 Derivation of the Nozzle flow profile : Single phase Adiabatic

For pressure ratio $PR = \dfrac{p_{out} + P_\infty}{p_0 + P_\infty}$ lower than crp1 and greater than crp2, a single stationary shock wave appears in the divergent. The flow description can be defined relatively to the the shock position. This position is obtained here by the use of dichotomy search protocol :

- As we knows that the shock is in the divergent, the initial guess for the shock cross section area is $A_C = \dfrac{A_* + A_{out}}{2}$. Where A_* is the throat area and A_{out} the outlet section area.
- Then the isentropic flow is solved from the inlet tank to the shock section.
- Rankine-Hugoniot relations are used across the shock to define the shocked state at the section immediately above the shock.
- The shocked state is connected to the outlet section with the help of isentropic solution.
- If the computed outlet pressure corresponds to the imposed one, the shock location is correct. Otherwise it has to be changed until the computed and imposed outlet pressure are the same.

This procedure converge fastly and an accurate location of the shock can be obtained after few iterations. Therefore the flow behind and ahead of the shock can be determined using the isentropic flow relations while keeping in mind that the states behind and ahead of the shock are linked by the Rankine-Hugoniot jump relations.

3.1.4 Solution examples

Exact solutions calculation is addressed with the following Laval nozzle geometry :
- Inlet cross section : 0.14657 m^2
- Throat cross section : 0.06406 m^2
- Outlet cross section : 0.14657 m^2

The nozzle's length is 1 m while the throat is located 0.5 m from the inlet.
The inlet is connected to a tank while the outlet is connected to a prescribed pressure. The fluid used in the calculations corresponds to liquid water, with the following SG EOS (2) parameters $\gamma = 4.4$, $P_\infty = 600MPa$. The tank state is defined by :

$$W_0 = \begin{pmatrix} \rho_0 = 1000\, Kg.m^{-3} \\ u_0 = 0\, m.s^{-1} \\ p_0 = 100MPa \end{pmatrix}$$

Figure (2) shows different typical solutions according by their respective pressure ratio $PR = \frac{p_{out} + P_\infty}{p_0 + P_\infty}$. For the present context, pressure ratios are respectively :
cpr1= 0.910388565776485,
cpr2= 0.245261271546139,
cpr3= 0.002679303212618317.
The pressure profiles corresponding to each pressure ratio are shown in the Figure 2. In addition, an isentropic pressure profile is shown in dashed lines for a subsonic flow in both convergent and divergent nozzle parts. It corresponds to the pressure ratio PR = 0.428571428571429. Another extra solution example is shown with a steady shock in the nozzle divergent. It corresponds to the pressure ratio PR = 0.934285714285714.

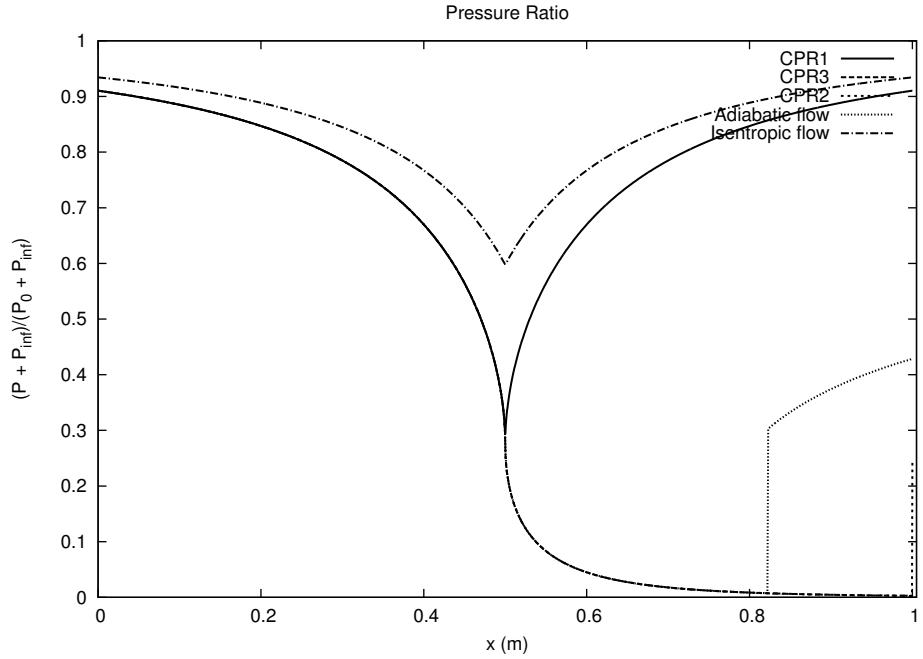

Figure 2: Dimensionless pressure profiles in the Laval nozzle for different exit pressures corresponding to subsonic flow with sonic throat (cpr1), supersonic isentropic flow (cpr3), flow with a steady shock in the exit section (cpr2), subsonic isentropic solution (PR = 0.428571428571429), adiabatic steady shock in the divergent (PR = 0.934285714285714).

3.1.5 Exact 1D nozzle solution with imposed mass flow rate and stagnation enthalpy

In many practical situations the inlet is not connected to a tank but has imposed inflow mass flow rate and stagnation enthalpy. In other words, the mass flux m_0 is imposed as well as the stagnation enthalpy H_0, corresponding to imposed total energy flux. The exact solution determination with such boundary conditions follows the same methodology as the one detailed previously with imposed tank conditions. We detail hereafter the subsonic isentropic solution only as it is the most important for the present study, that focuses on low Mach number flows.

Derivation of the outlet section state The outlet pressure is described as previously and denoted by p_{out}. Thanks to this information, the entire state can be determined in the outlet section. Relations (8) and the mass flow rate conservation between the inlet and the outlet sections yield:

$$\begin{aligned} &\frac{\gamma\left(p_{out}+P_\infty\right)}{\left(\gamma-1\right)\rho_{out}}+\frac{1}{2}u_o^2=H_0 \\ &m_0=\rho_0 u_0 A_0=\rho_{out}U_{out}A_{out}=P_{out} \end{aligned} \tag{26}$$

Combining these two relations, a non-linear function of the specific volume, $v_{out}=\dfrac{1}{\rho_{out}}$, in the outlet section is obtained:

$$\frac{1}{2}\left(\frac{m_0A_0}{A_{out}}\right)^2 v_{out}^2+\frac{\gamma(p_{out}+P_\infty)}{(\gamma-1)}v_{out}-H_0=0 \tag{27}$$

This equation admits two roots but only one is positive :

$v_{out}=2\left(\dfrac{A_{out}}{m_0A_0}\right)^2\left(\sqrt{\Delta}-\dfrac{\gamma(p_{out}+P_\infty)}{(\gamma-1)}\right)$

where $\Delta=\left(\dfrac{\gamma(p_{out}+P_\infty)}{(\gamma-1)}\right)^2+2\left(\dfrac{m_0A_0}{A_{out}}\right)^2 H_0$

Once the specific volume in the outlet is known, the outlet velocity, U_{out}, is determined from the mass flow rate conservation.

Computation of the state at a given section Relations (8) and (**??**) are expressed between the outlet state and a given point with cross section A_i.

$$\frac{\gamma(p_i+P_\infty)}{(\gamma-1)\rho_i}+\frac{1}{2}u_i^2=H_o \tag{28}$$

$$\frac{p_i+P_\infty}{\rho_i^\gamma}=\frac{p_{out}+P_\infty}{\rho_o^\gamma} \tag{29}$$

The system is closed by the mass conservation equation:

$$\rho_i u_i A_i=m_0 \tag{30}$$

Using relation (29) to express ρ_i in (30) and (28), the following non-linear relation is obtained:

$$\frac{\gamma(p_{out}+P_\infty)^{\frac{1}{\gamma}}}{(\gamma-1)\rho_{out}}\left(p_i+P_\infty\right)^{\frac{\gamma-1}{\gamma}}+\left(\frac{m_0}{A_i\rho_{out}}\right)^2\left(p_{out}+P_\infty\right)^{\frac{2}{\gamma}}\left(p_i+P_\infty\right)^{\frac{-2}{\gamma}}-H_o=0 \tag{31}$$

Once p_i is determined, ρ_i is determined by (29) and u_i is deduced by (30).

3.1.6 Comparison of the low Mach number compressible exact solution and the incompressible exact one

In the first part of this section, incompressible exact solution determination is addressed. In the second part this exact solution is compared to the compressible exact one detailed previously.

Incompressible exact solution For incompressible flows, the mass flux conservation and the Bernoulli relation expressed between the inlet and the outlet section read :

$$A_0 u_0 = A_{out} U_{out} \quad \text{and} \quad p_0 + \frac{1}{2}\rho u_0^2 = p_{out} + \frac{1}{2}\rho U_{out}^2 \tag{32}$$

Combining this two relations the following identity is obtained :

$$p_0 = p_{out} + \frac{1}{2}\rho u_0^2 \left(\left(\frac{A_0}{A_{out}} \right)^2 - 1 \right) \tag{33}$$

The mass flux $m_0 = \rho A_0 u_0$ is given as well as the outlet pressure p_{out}. As the density ρ is constant and the outlet section A_0 is given, the inflow velocity is readily obtained $u_0 = \dfrac{m_0}{\rho A_0}$. Consequently, the inflow pressure in determined from (33).
The solution at a given point of cross section A_i, is determined from the following two relations :

$$u_i = \frac{A_0}{A_i} u_0 \quad \text{and} \quad p_i = p_0 + \frac{1}{2}\rho u_0^2 \left(1 - \left(\frac{A_0}{A_i} \right)^2 \right) \tag{34}$$

Comparison with the compressible exact solution under low Mach conditions The figures 3, 4 and 5 show the low Mach number compressible exact solution versus the incompressible exact one. The fluid used corresponds to liquid water while the imposed mass flow rate, m, is equal to $7000 Kg.m^{-2}.s^{-1}$ and the imposed stagnation enthalpy H is computed using $P = 1.0 Bar$ and $\rho = 1000 Kg.m^{-3}$. The geometrical data are those given in Section 3.1.4. The two first graphs show perfect agreement between compressible and incompressible pressure and velocity fields as the flow maximum Mach number is 0.01 . The density profile show slight deviations. The incompressible solution is obviously constant while the compressible one shows variations of about $10^{-5}\rho_0$.

We can thus conclude that in the low Mach regime both exact solutions are in close agreement. The exact single phase nozzle flow solution being now in hand, it is interesting to check the accuracy of existing numerical methods against these reference solutions.

3.1.7 Behavior of conventional Godunov type schemes in low Mach number conditions

The Godunov scheme for the Euler equations in ducts of smooth varying cross section is considered for the computation of steady liquid nozzle flows. This scheme, with HLLC approximate Riemann solver, is summarized in the Appendix 6 . Computed results are compared with the exact nozzle solution under low Mach number flow conditions, for various meshes of increasing refinement : 100, 1000 and 10,000 cells. The corresponding results are shown in the Figures 6, 7 and 8, again with the same geometrical nozzle parameters as those of the preceding subsection.

The computed and exact velocity profiles are in perfect agreement. This is not the case of the pressure field that shows 500% error, due to density fluctuations combined with the SG EOS (2) stiffness. Under mesh refinement the error decreases and quasi convergence is reached with 10,000 cells. Table 1 shows computational time to reach steady state versus mesh size. It is clear that the method is extremely expensive, even for 1D computations.

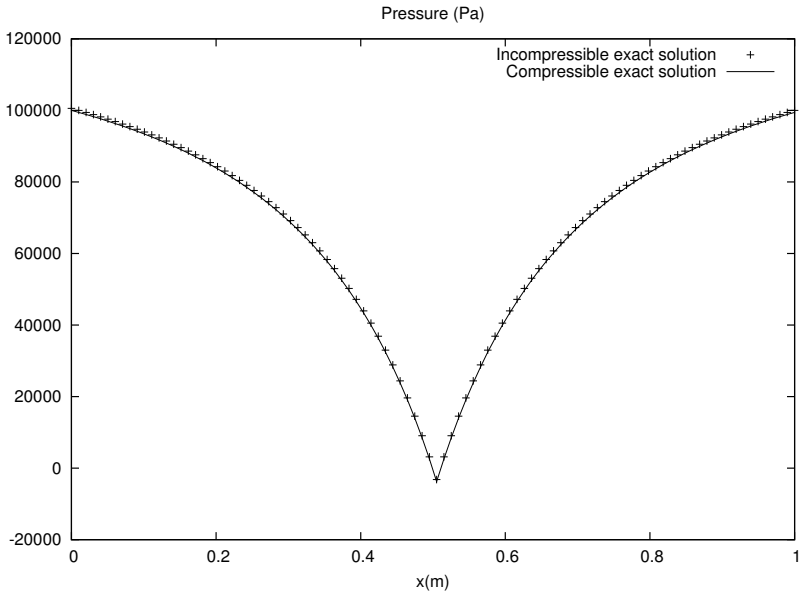

Figure 3: Compressible and incompressible exact solutions : pressure profiles. The two solutions are merged.

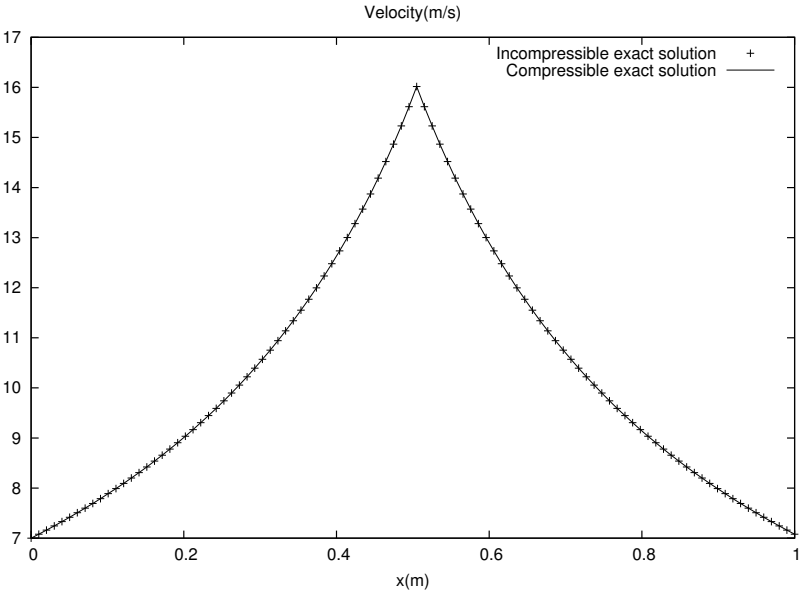

Figure 4: Compressible and incompressible exact solutions : velocity profiles. The two solutions are merged.

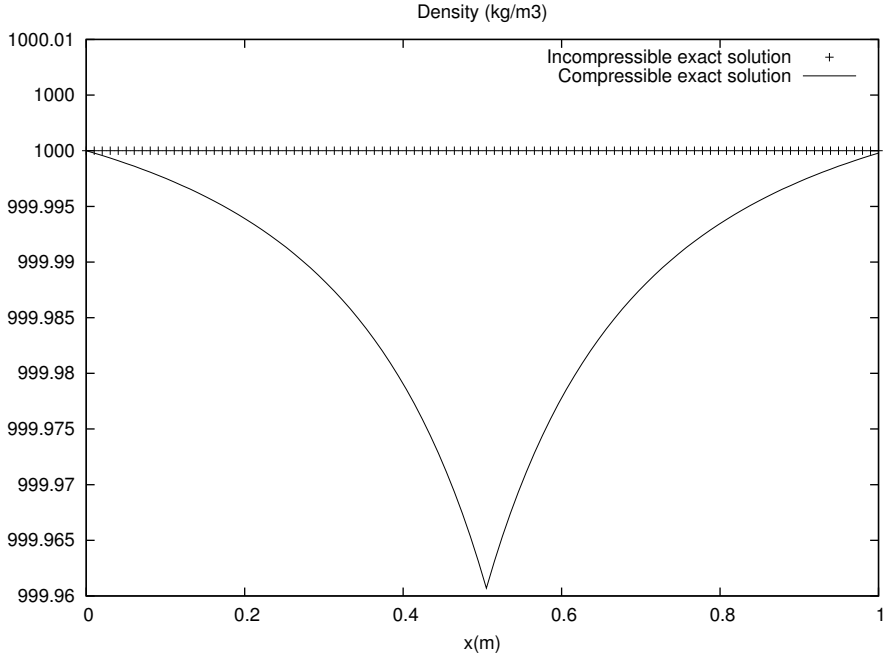

Figure 5: Compressible and incompressible exact solutions : density profiles. The compressible exact solution obviously slightly differs from the incompressible exact one.

Mesh size	Calculation time
100 cells	20 s
1000 cells	33 min 56 s
10000 cells	59 h 16 min 48 s

Table 1: Computational time versus mesh size.

3.2 Two-phase nozzle flows

We now consider the same nozzle flow problem as the one depicted in the figure (1) but in the context of the Kapila et al. flow model [19]. For smooth solutions, system (3) admits two extra conservation laws,

$$\frac{\partial \alpha_1 \rho_1 s_1}{\partial t} + \frac{\partial \alpha_1 \rho_1 s_1 u}{\partial x} = 0, \tag{35}$$

$$\frac{\partial \alpha_2 \rho_2 s_2}{\partial t} + \frac{\partial \alpha_2 \rho_2 s_2 u}{\partial x} = 0, \tag{36}$$

that will be of particular use in the following. Each fluid is assumed governed by the SG EOS (2) and the mixture evolves in pressure equilibrium : $p_1 = p_2$. The tanks state is now defined by :

$$W_0 = (\rho_0,\ u_0,\ \alpha_{1,0},\ Y_{1,0},\ P_0)^T \text{ , where } Y_k = \frac{\alpha_k \rho_k}{\rho}$$

or equivalently by $W_0 = (\rho_{1,0},\ \rho_{2,0},\ u_0,\ \alpha_{1,0},\ P_0)^T$

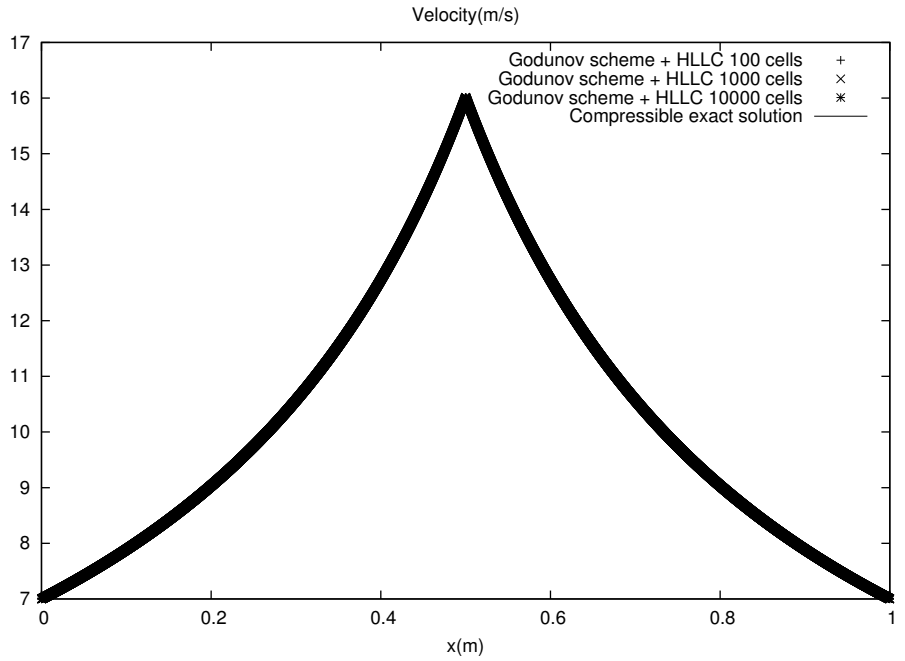

Figure 6: Computed velocity profiles with 100, 1000 and 10,000 cells against the compressible exact solution. The four solutions are merged.

3.2.1 Critical pressure ratios

The various flow regimes occurring in the Laval nozzle are related, as previously for single phase flows, to the outlet/inlet pressure ratio.

Critical pressure ratio 1 (cpr1) In this flow regime, the throath has a sonic state, while it is subsonic elsewhere. To determine the throath pressure associated to the sonic state, the following relations are used:

$$H_* = H_0, \tag{37}$$

$$s_{1,*} = s_{1,0}, \tag{38}$$

$$s_{2,*} = s_{2,0}, \tag{39}$$

$$Y_{1,*} = Y_{1,0}, \tag{40}$$

$$Y_{2,*} = Y_{2,0}, \tag{41}$$

$$u_* = c_*. \tag{42}$$

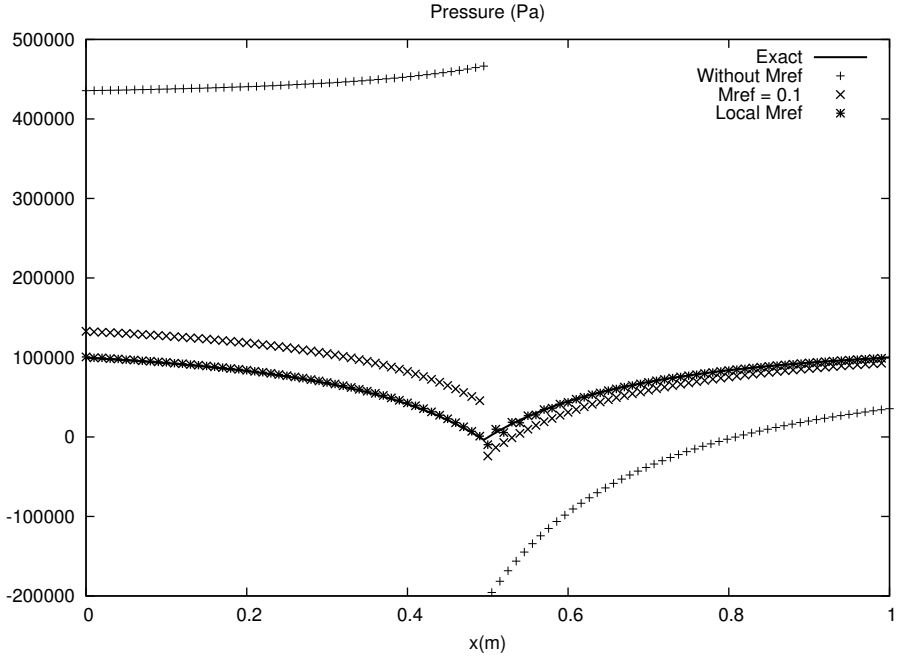

Figure 7: Computed pressure profiles in the Laval nozzle with 100, 1000 and 10,000 cells against the compressible exact solution. The Godunov scheme with coarse mesh predicts a solution with a factor 5 error. This error decreases under mesh refinement. Quasi-converged results are obtained for the 10,000 cells mesh.

The total enthalpy is defined by : $H = Y_1 h_1 + Y_2 h_2 + \dfrac{1}{2}u^2$. These various relations are expressed as functions of the pressure :

$$Y_{1,0} h_{1,*}(P_*) + Y_{2,0} h_{2,*}(P_*) + \frac{1}{2} c_*^2(P_*) = h_0 \tag{43}$$

with $h_{k,*} = \dfrac{\gamma_k (P_* + P_{\infty,k})}{(\gamma_k - 1)\rho_{k,*}}$.
The isentropes are expressed as :

$$\rho_{k,*} = \rho_{k,*}(P_*) = \rho_{k,0} \left(\frac{P_* + P_{\infty,k}}{P_0 + P_{\infty,k}} \right)^{\dfrac{1}{\gamma_k}} \tag{44}$$

The sound speed of System (3) corresponds to the Wood [45] one :

$$\frac{1}{\rho_* c_*^2} = \frac{\alpha_{1,*}}{\rho_{1,*} c_{1,*}^2} + \frac{\alpha_{2,*}}{\rho_{2,*} c_{2,*}^2} \tag{45}$$

In this relation, the mixture density is determined by :

$$\frac{1}{\rho_*} = \frac{Y_{1,0}}{\rho_{1,*}(P_*)} + \frac{Y_{2,0}}{\rho_{2,*}(P_*)} \tag{46}$$

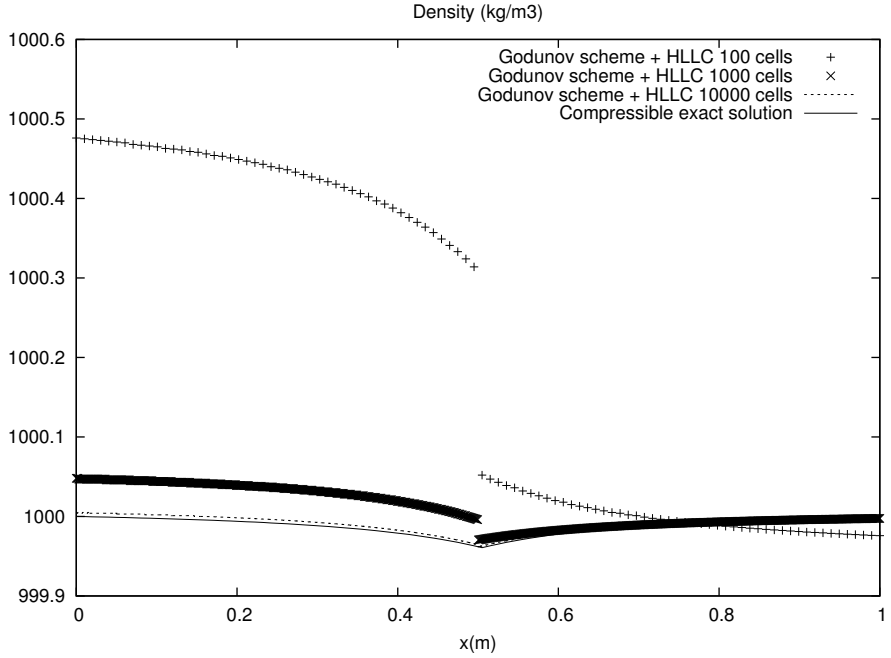

Figure 8: Computed density profiles in the Laval nozzle with 100, 1000 and 10,000 cells against the compressible exact solution. The Godunov scheme solutions present some fluctuations. The error decreases under mesh refinement.

The squared sound speeds are given by their definition :

$$c_{k,*}^2 = \gamma_k \frac{P_* + P_{\infty,k}}{\rho_{k,*}(P_*)} \tag{47}$$

The volume fractions $\alpha_{k,*}$ are determined from the mass fractions definition :

$$\alpha_{k,*} = \frac{Y_{k,0}\rho_*(P_*)}{\rho_{k,*}(P_*)} \tag{48}$$

All these relations are used in Relation (43) that forms a non-linear function of P_*. Is is solved by the Newton-Raphson method. Once the star pressure is determined, all subsequent variables at the sonic throath are determined.

There is thus no difficulty to determine the first critical pressure ratio (cpr1). To do so, the mass flow rate is expressed at throath,

$$m_* = \rho_* u_* A_* \tag{49}$$

This mass flow rate is the same in the outlet section. Thus, the velocity in the outlet section reads,

$$U_{out}(P_{out}) = \frac{m_* v_{out}(P_{out})}{A_{out}} \tag{50}$$

where the outlet pressure P_{out} has to be determined. The specific volumes at the outlet section are given by :

$$v_{k,out} = v_{k,0} \left(\frac{P_0 + P_{\infty,k}}{P_{out} + P_{\infty,k}} \right)^{\frac{1}{\gamma_k}} \tag{51}$$

and the mixture specific volume reads,

$$v_{out} = Y_{1,0} v_{1,out}(P_{out}) + Y_{2,0} v_{2,out}(P_{out}). \tag{52}$$

These relations are inserted in the total enthalpy conservation expressed between the tank and the outlet section :

$$Y_{1,0} h_{1,out}(P_{out}) + Y_{2,0} h_{2,out}(P_{out}) + \frac{1}{2} u^2_{out}(P_{out}) - h_0 = 0 \tag{53}$$

This equation admits two roots. To determine the critical pressure ratio cpr1, the Newton method is initialized with $P_{out} = P_*$. Once P_{out} is determined, the critical pressure ratio is deduced as:

$$cpr1 = \frac{P_{out}}{P_0} = \frac{P_{cpr1}}{P_0} \tag{54}$$

Critical pressure ratio 3 (cpr3) The same relation (53) is solved with the Newton method taking $P_{out} = (1 + 10^{-6}) Min(P_{\infty,1}, P_{\infty,2})$ as initial guess for the outlet pressure.Once P_{out} is determined, the critical pressure ratio is deduced as :

$$cpr3 = \frac{P_{out}}{P_0} = \frac{P_{cpr3}}{P_0} \tag{55}$$

Critical pressure ratio 2 (cpr2) This pressure ratio is associated to the pressure corresponding to a steady shock wave in the outlet section. Thus, the flow enters the shock at a pressure equal to P_{cpr3}. The shock jump relations [36] are used:

$$(\rho u)_{cpr3} = (\rho u)_{cpr2} \tag{56}$$

$$\left(\rho u^2 + P\right)_{cpr3} = \left(\rho u^2 + P\right)_{cpr2} \tag{57}$$

$$e_{1,cpr2} - e_{1,cpr3} + \frac{P_{cpr2} + P_{cpr3}}{2} \left(v_{1,cpr2} - v_{1,cpr3}\right) = 0 \tag{58}$$

$$e_{2,cpr2} - e_{2,cpr3} + \frac{P_{cpr2} + P_{cpr3}}{2} \left(v_{2,cpr2} - v_{2,cpr3}\right) = 0 \tag{59}$$

Inserting the SG EOS in these two last relations, the specific volumes are expressed as functions of the shock state pressure :

$$\frac{v_{1,cpr2}}{v_{1,cpr3}} = \frac{(\gamma_1 - 1)(P_{cpr2} + P_{\infty,1}) + (\gamma_1 + 1)(P_{cpr3} + P_{\infty,1})}{(\gamma_1 - 1)(P_{cpr3} + P_{\infty,1}) + (\gamma_1 + 1)(P_{cpr2} + P_{\infty,1})} \tag{60}$$

$$\frac{v_{2,cpr2}}{v_{2,cpr3}} = \frac{(\gamma_2 - 1)(P_{cpr2} + P_{\infty,2}) + (\gamma_2 + 1)(P_{cpr3} + P_{\infty,2})}{(\gamma_2 - 1)(P_{cpr3} + P_{\infty,2}) + (\gamma_2 + 1)(P_{cpr2} + P_{\infty,2})} \tag{61}$$

Combining Relations (56) and (57), the following relation is obtained,

$$P_{cpr2} = P_{cpr3} + \rho_{cpr3} + \rho_{cpr3} u_{cpr3}^2 \left(1 - \frac{v_{cpr2}}{v_{cpr3}}\right). \tag{62}$$

The mixture specific volume v_{cpr2} can be expressed as a function of the pressure P_{crp2} as :

$$v_{crp2} = Y_{1,0} v_{1,crp2}(P_{crp2}) + Y_{2,0} v_{2,crp2}(P_{crp2}) \tag{63}$$

Combining these two last relations, a non-linear function of P_{crp2} is obtained.
It is solved by the Newton-Raphson method by taking $P_{crp2} = P_{crp1}$ as initial guess. The critical pressure ratio $cpr2$ is then deduced as :

$$cpr2 = \frac{P_{out}}{P_0} \tag{64}$$

3.2.2 Derivation of the Nozzle flow profile : two-phase isentropic

As for the single phase case, the flow is isentropic when the pressure ratio $PR = \dfrac{P_{out}}{P_0}$ is either greater than $cpr1$ or lower than $crp2$. The outlet pressure P_{out} is imposed by the boundary conditions and the remaining state variables can be determined from :

$$\rho_{1,out} = \rho_{1,0} \left(\frac{P_{out} + P_{\infty,1}}{P_0 + P_{\infty,1}}\right)^{\frac{1}{\gamma_1}} \tag{65}$$

$$\rho_{2,out} = \rho_{2,0} \left(\frac{P_{out} + P_{\infty,2}}{P_0 + P_{\infty,2}}\right)^{\frac{1}{\gamma_2}} \tag{66}$$

$$v_{out} = Y_{1,0} v_{1,out} + Y_{2,0} v_{2,out} \tag{67}$$

$$h_{1,out} = \frac{\gamma_1 \left(P_{out} + P_{\infty,1}\right)}{\left(\gamma_1 - 1\right) \rho_{1,out}} \tag{68}$$

$$h_{2,out} = \frac{\gamma_1 \left(P_{out} + P_{\infty,2}\right)}{\left(\gamma_2 - 1\right) \rho_{2,out}} \tag{69}$$

$$\alpha_{k,out} = \frac{Y_{k,0} \rho_{out}(P_{out})}{\rho_{k,out}(P_{out})} \tag{70}$$

The velocity at the outlet is determined from the total enthalpy definition :

$$U_{out} = \sqrt{2\left[h_0 - \left(Y_{1,0} h_{2,out}(P_{out}) + Y_{2,0} h_{2,out}(P_{out})\right)\right]} \tag{71}$$

From the outlet state knowledge, there is no difficulty to determine the mixture mass flow rate :

$$m = \rho_{out} U_{out} A_{out} \tag{72}$$

In a given area of cross section A_i, the velocity reads:

$$u_i = \frac{m v_i(P_i)}{A_i}, \tag{73}$$

where the pressure P_i has to be determined. The total enthalpy conservation expressed between the tank and the A_i section reads,

$$Y_{1,0}h_{1,i}(P_i) + Y_{2,0}h_{2,i}(P_i) + \frac{1}{2}u^2(P_i) - h_0 = 0 \tag{74}$$

where the enthalpies $h_{1,i}$ and $h_{2,i}$ are deduced from the same set of relations (65 - 69). Relation (74) is solved by the Newton-Raphson method with $P_i = P_0$ as the initial guess in the nozzle convergent and $P_i = P_{out}$ in the nozzle divergent. Once the pressure P_i is determined, the volume fractions are determined by the same relations (70).

3.2.3 Derivation of the Nozzle flow profile : two-phase Adiabatic

When the pressure ratio, $PR = \dfrac{P_{out}}{P_0}$ is lower than crp1 and greater than crp2 a steady shock wave appears in the divergent. To determine the shock position we use the same method as previously, for single phase nozzle flows, except that the Rankine-Hugoniot jump relations correspond now to System (56-59).

3.2.4 Solution examples

The exact solutions calculation is addressed with the same geometry as previously (cf Section 3.1.4). The fluids used in the calculations corresponds to liquid water and air, with the following SG EOS (2) parameters $\gamma_{water} = 4.4$, $P_{\infty,water} = 600MPa$, $\gamma_{air} = 1.4$, $P_{\infty,air} = 0Pa$. The tank state is defined by :

$$W_0 = \begin{pmatrix} \rho_{1,0} = 1000\, Kg.m^{-3} \\ \rho_{2,0} = 1\, Kg.m^{-3} \\ u_0 = 0\, m.s^{-1} \\ \alpha_{1,0} = 0.99999 \\ P_0 = 1\, MPa \end{pmatrix}.$$

Where subscripts "1" and "2" correspond to the water and the air, respectively. Figure (9) shows different typical solutions according by their respective pressure ratio $PR = \dfrac{P_{out}}{P_0}$. In this case, critical pressure ratios are respectively :
cpr1= 0.80973973,
cpr2= 0.40989492,
cpr3= $6.9815930.10^{-8}$.
The pressure profiles corresponding to each pressure ratio are shown in the Figure 9. In addition, an isentropic pressure profile is shown in dashed lines for a subsonic flow in both convergent and divergent nozzle parts. It corresponds to the pressure ration PR = 0.9. An extra solution example is shown with a steady shock in the nozzle divergent. It corresponds to the pressure ratio PR = 0.5. Furthermore, Mach number and water volume fraction profiles are shown in the Figures 10, 11 and 12. The sonic state at throath appears for weak pressure ratios ($cpr \leq 0.8$) which are quite easy to reach in practical systems. From that pressure ratio, when the outlet pressure is lowered (or the tank pressure is increased) part of the divergent is supersonic. The Mach number increases dramatically, as the sound speed is non monotonic versus volume fraction. Thus, the gas volume fraction increases as the pressure decreases and cavitation zones appear. It is worth to mention that the the obtained cavitating nozzle flow is "ideal" or "academic", at least for two reasons:

1) The cavitation zone that appears in the divergent is not due to liquid-gaz phase change but only to bubbles growth, imposed by the pressure equilibrium condition.

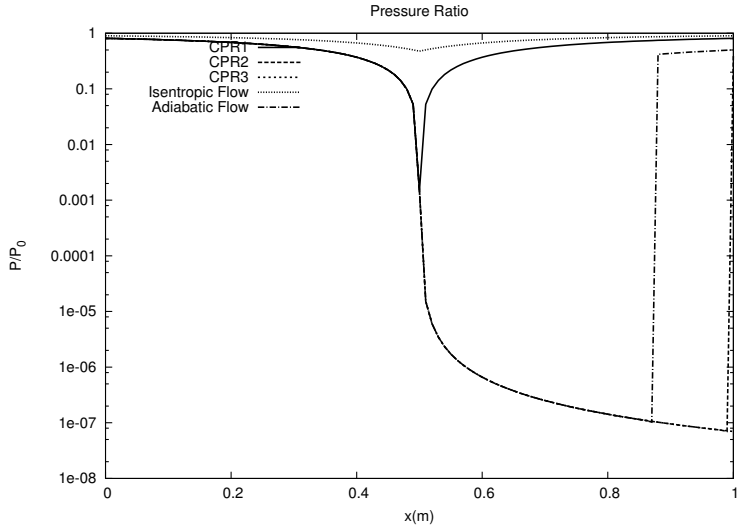

Figure 9: Dimensionless pressure profiles in the Laval nozzle for different exit pressures corresponding to subsonic flow with sonic throat (cpr1), supersonic isentropic flow (cpr3), flow with a steady shock in the exit section (cpr2), subsonic isentropic solution (PR = 0.9) and steady shock in the divergent (PR = 0.5).

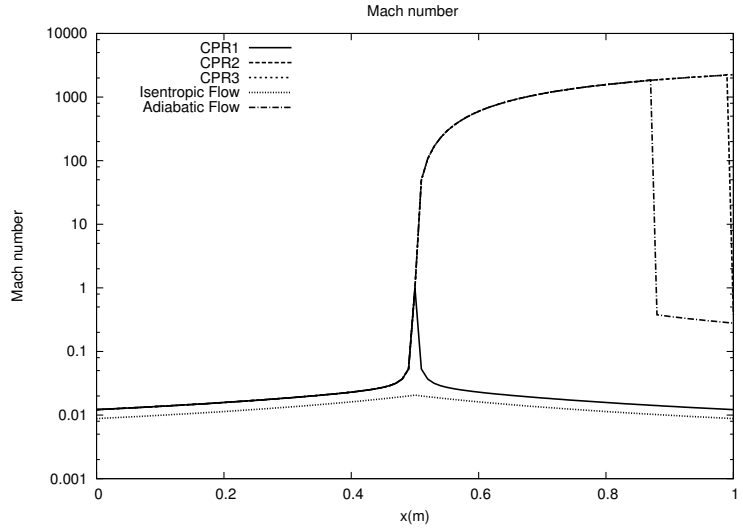

Figure 10: Mach number profiles in the Laval nozzle for different exit pressures corresponding to subsonic flow with sonic throat (cpr1), supersonic isentropic flow (cpr3), flow with a steady shock in the exit section (cpr2), subsonic isentropic solution (PR = 0.9) and steady shock in the divergent (PR = 0.5).

2) The reference solution derived previously is 1D whereas experimental ones always deal with multi-D effects. Indeed, cavitation zones correspond to multi-D pockets, separating a

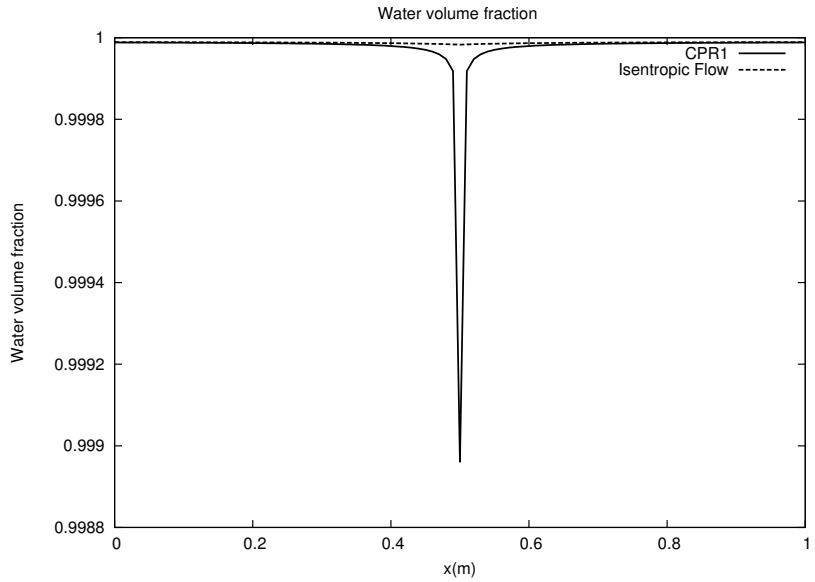

Figure 11: Water volume fraction profiles in the Laval nozzle for different exit pressures corresponding to subsonic flow with sonic throat (cpr1) and subsonic isentropic solution (PR = 0.9).

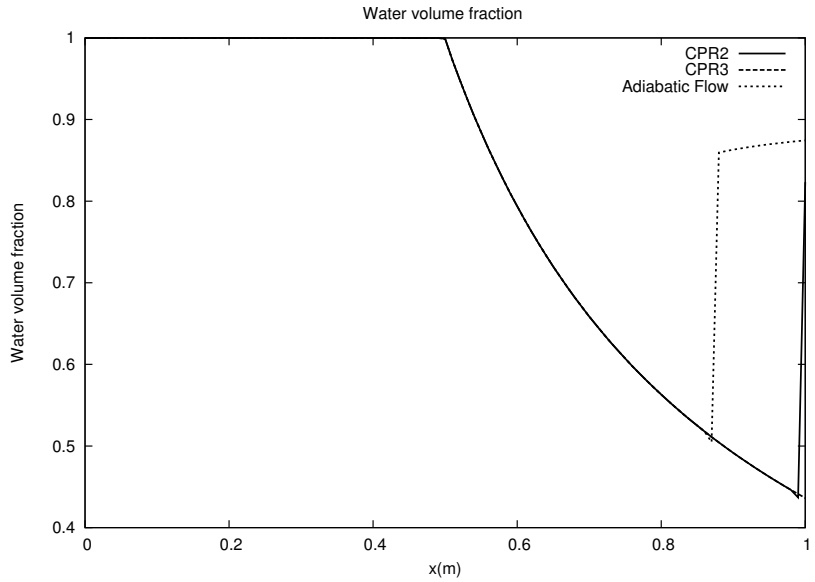

Figure 12: Volume fraction of water profiles in the Laval nozzle for different exit pressures corresponding to supersonic isentropic flow (cpr3), flow with a steady shock in the exit section (cpr2) and steady shock in the divergent (PR = 0.5).

nearly pure gas and a nearly pure liquid in the nozzle.

These multi-D effects also imply velocity disequilibrium in a given cross-section. The two-phase reference solution derived previously is however clearly helpful to examine the accuracy and convergence of numerical schemes of two-phase nozzle flows computations.

3.2.5 Exact two-phase nozzle solution with imposed mass flow rate and stagnation enthalpy

In many practical situations the inlet is not connected to a tank but has imposed mass inflow and stagnation enthalpy. In other words, the mass flux m_0 is imposed as well as the stagnation enthalpy H_0, corresponding to imposed total energy flux. For two-phase flows, the mixture enthalpy reads:

$$H_0 = Y_{0,1}h_{0,1} + Y_{0,2}h_{0,2} + \frac{1}{2}u_0^2 \tag{75}$$

It means that the mass fractions have to be imposed, as well as the volume fraction of one of the phase, $\alpha_{0,1}$, for example. It is thus necessary to impose m_0, $h_{k,0}$, $Y_{k,0}$. Another option being to impose m_0, P_0, $\rho_{k,0}$ and $\alpha_{1,0}$. The exact solution determination with such boundary conditions follows the same methodology as the one detailed previously with imposed tank conditions. We detail hereafter the subsonic isentropic solution only as it is the most important for the present study, that focuses on low Mach number flows.

Outlet state determination The outlet pressure is prescribed as previously and denoted by P_{out}. Using the SG EOS (2) the phase total enthalpy is expressed as follows:

$$h_k = \frac{\gamma_k(P + P_{\infty,k})v_k}{(\gamma_k - 1)} + \frac{1}{2}u^2 \tag{76}$$

Thus, using the phase total enthalpy conservation between the inlet and the outlet (as we focus only on the subsonic isentropic solution), we obtain:

$$h_{k,0} = \frac{\gamma_k(P_{out} + P_{\infty,k})v_{k,out}}{(\gamma_k - 1)} + \frac{1}{2}u_{out}^2 \tag{77}$$

With the help of the mass flow rate conservation ($m_0 = \rho_{out}A_{out}U_{out}$) and the mixture density definition ($\frac{1}{\rho_{out}} = Y_{1,0}v_{1,out} + Y_{2,0}v_{2,out}$), the two following equations are obtained:

$$h_{1,0} = \frac{\gamma_1(P_{out} + P_{\infty,1})v_{1,out}}{(\gamma_1 - 1)} + \frac{1}{2}\left(\frac{m_0}{A_{out}}\right)^2 (Y_{1,0}v_{1,out} + Y_{2,0}v_{2,out})^2 \tag{78}$$

$$h_{2,0} = \frac{\gamma_2(P_{out} + P_{\infty,2})v_{2,out}}{(\gamma_2 - 1)} + \frac{1}{2}\left(\frac{m_0}{A_{out}}\right)^2 (Y_{1,0}v_{1,out} + Y_{2,0}v_{2,out})^2 \tag{79}$$

Combining these two relations, we obtain a expression linking $v_{1,out}$ and $v_{2,out}$:

$$v_{1,out} = \frac{(\gamma_1 - 1)}{\gamma_1(P_{out} + P_{\infty,1})}\left[h_{1,0} - h_{2,0} + \frac{\gamma_2(P_{out} + P_{\infty,2})v_{2,out}}{(\gamma_2 - 1)}\right] \tag{80}$$

Using this expression in Relation (79) a second order polynomial in $v_{2,out}$ is obtained. Keeping the positive solution, $v_{1,out}$ is obtained using (80). Once $v_{1,out}$ and $v_{2,out}$ are known, the mixture density at the outlet section is obtained by,

$$\frac{1}{\rho_{out}} = Y_{1,0}v_{1,out} + Y_{2,0}v_{2,out} \tag{81}$$

and the outlet velocity is deduced by,

$$U_{out} = \frac{m_0}{\rho_{out} A_o}. \tag{82}$$

Last, the volume fractions are determined with the help of mass fractions conservation,

$$\alpha_{k,0} = Y_{k,0} \rho_{out} v_{k,out}. \tag{83}$$

Variables state determination in an arbitrary area As the flow is isentropic between a section of arbitrary area (A) and the outlet section, the phase density can be expressed using relations (65 - 66) between the outlet and a section of arbitrary area. Thus, writing the phase total enthalpy conservation between a section of arbitrary area and the outlet gives the following relation:

$$h_{k,out} = \frac{\gamma_k (P + P_{\infty,k}) v_k(P)}{(\gamma_k - 1)} + \frac{1}{2} \left(\frac{m_0}{A} \right)^2 \left(Y_{1,0} v_{1,out}(P) + Y_{2,0} v_{2,out}(P) \right)^2 \tag{84}$$

The mixture pressure, P, is therefore determined by solving one of these relations using the Newton-Raphson method. Once P is known, the phase densities are determined using (65 - 66) while the other variables are computed as previously.

4 Improving numerical convergence in the low Mach number limit

We now address the numerical approximation of flow models (1) and (3) corresponding to single fluid and two-phase fluid respectively. For the sake of simplicity, the analysis is carried out in 1D, multi-D extension being addressed later.

4.1 Low Mach number preconditioning

As shown previously, the conventional Godunov method converges to the exact low Mach number solution if very fine resolution is used. Such meshes being impracticable for multi-dimensional applications, modifications have to be done. We are seeking a numerical method valid for all speeds flows, from transonic to low Mach number. Transonic and high Mach number conditions require conservative formulation of the equations and corresponding numerical scheme. In this area, Riemann problem based methods are recommended. The difficulty with conservative formulations is to reach the incompressible limit when the Mach number tends to zero as it is well known that corresponding solvers fail to provide an accurate approximation of the incompressible equations. It seems that the acoustic dissipation process is not efficient enough for finite volumes approximations using Riemann solvers. Indeed, Riemann solvers are based on acoustic linearization, which aims to slowly dissipate acoustic waves. Therefore, Riemann solvers preconditioning is needed to manage the numerical dissipation in order to improve the numerical convergence at low Mach number limit. In order to achieve this goal, Turkel [43] proposed to enforce pressure time invariance up to Mach number square fluctuations with the help of a penalization method. *In the context of Riemann solvers, this penalization can be applied to modify the Riemann problem solution while the conservative formulation and real equation of state are still used during the solution update.* This strategy is presented hereafter in the context of the Euler equations first, the multiphase flow formulation being addressed latter. The HLLC Riemann solver of Toro et al. [42] is considered and wave's speeds for all Mach number flow situations are estimated following

Braconnier and Nkonga [6] with the help of the following analysis. For the approximate Riemann problem resolution, the Euler equations are considered under primitive variables formulation:

$$\begin{aligned}
&\frac{\partial \rho}{\partial t} + \rho \frac{\partial u}{\partial x} + u \frac{\partial \rho}{\partial x} = 0 \\
&\frac{\partial u}{\partial t} + u \frac{\partial u}{\partial x} + \frac{1}{\rho} \frac{\partial p}{\partial x} = 0 \\
&\frac{\partial p}{\partial t} + u \frac{\partial p}{\partial x} + \rho c^2 \frac{\partial u}{\partial x} = 0
\end{aligned} \tag{85}$$

4.1.1 Dimensionless variables

These equations are expressed in dimensionless variables with the help of the following definitions : $\rho = [\rho]\tilde{\rho}$, $u = [u]\tilde{u}$, $p = [p]\tilde{p}$, $x = [x]\tilde{x}$ and $t = [t]\tilde{t}$, where $[f]$ represents a characteristic scale of the corresponding variable and $\tilde{f}$ the dimensionless one. System (85) becomes :

$$\begin{aligned}
&\frac{\partial \tilde{\rho}}{\partial \tilde{t}} + \tilde{\rho} \frac{\partial \tilde{u}}{\partial \tilde{x}} + \tilde{u} \frac{\partial \tilde{\rho}}{\partial \tilde{x}} = 0 \\
&\frac{\partial \tilde{u}}{\partial \tilde{t}} + \tilde{u} \frac{\partial \tilde{u}}{\partial \tilde{x}} + \frac{[p]}{[\rho][u]^2 \tilde{\rho}} \frac{\partial \tilde{p}}{\partial \tilde{x}} = 0 \\
&\frac{\partial \tilde{p}}{\partial \tilde{t}} + \tilde{u} \frac{\partial \tilde{p}}{\partial \tilde{x}} + \frac{[\rho][c]^2}{[p]} \tilde{\rho} \tilde{c}^2 \frac{\partial \tilde{u}}{\partial \tilde{x}} = 0
\end{aligned} \tag{86}$$

A pressure scaling has to defined. At least, two options are possible:
- An 'acoustic' scaling, corresponding to,

$$[p] = [\rho][c][u] \tag{87}$$

- A 'bulk modulus' scaling, corresponding to,

$$[p] = [\rho][c]^2 \tag{88}$$

These different pressure scales result in two dimensionless Euler equations. The existence of these two branches is precisely at the basis of conventional algorithms convergence difficulties. As illustrated in the Figures (7 - 8) the Godunov scheme has low dissipation of the acoustics scale and consequently presents convergence issues. As shown in the next subsection, the 'bulk modulus scaling',

$$\begin{aligned}
&\frac{\partial \tilde{\rho}}{\partial \tilde{t}} + \tilde{\rho} \frac{\partial \tilde{u}}{\partial \tilde{x}} + \tilde{u} \frac{\partial \tilde{\rho}}{\partial \tilde{x}} = 0 \\
&\frac{\partial \tilde{u}}{\partial \tilde{t}} + \tilde{u} \frac{\partial \tilde{u}}{\partial \tilde{x}} + \frac{1}{M^2 \tilde{\rho}} \frac{\partial \tilde{p}}{\partial \tilde{x}} = 0 \\
&\frac{\partial \tilde{p}}{\partial \tilde{t}} + \tilde{u} \frac{\partial \tilde{p}}{\partial \tilde{x}} + \tilde{\rho} \tilde{c}^2 \frac{\partial \tilde{u}}{\partial \tilde{x}} = 0,
\end{aligned} \tag{89}$$

formally admits the incompressible Euler equations as asymptotic limit when the Mach number tends to zero. We thus consider System (89) in the following where the symbol $\sim$ is dropped for the sake of simplicity.

4.1.2 Asymptotic analysis

We now examine the limit system associated to System (89) when the Mach number tends to zero. To do so, an asymptotic analysis is done. The various flow variables 'f' are expanded as:

$$f = f_0 + \epsilon f_1 + \epsilon^2 f_2, \qquad \text{where } \epsilon \to 0^+.$$

A the order ϵ^{-2} System (89) implies,

$$\frac{\partial p_0}{\partial x} = 0 \tag{90}$$

A the order ϵ^{-1} it implies,

$$\frac{\partial p_1}{\partial x} = 0 \tag{91}$$

and at leading order the limit system reads:

$$\begin{aligned} &\frac{\partial \rho_0}{\partial t} + u_0 \frac{\partial \rho_0}{\partial x} + \rho_0 \frac{\partial u_0}{\partial x} = 0 \\ &\frac{\partial u_0}{\partial t} + u_0 \frac{\partial u_0}{\partial x} + \frac{1}{\rho_0} \frac{\partial p_2}{\partial x} = 0. \\ &\frac{\partial p_0}{\partial t} + \rho_0 c_0^2 \frac{\partial u_0}{\partial x} = 0 \end{aligned} \tag{92}$$

Under the condition,

$$\frac{\partial p_0}{\partial t} = 0, \tag{93}$$

System (92) tends formally to the incompressible Euler equations when the Mach number tends to zero. Indeed, the incompressible Euler equations read:

$$\begin{aligned} &\rho_0 = const. \\ &\frac{\partial u_0}{\partial x} = 0 \\ &\frac{\partial u_0}{\partial t} + u_0 \frac{\partial u_0}{\partial x} + \frac{1}{\rho_0} \frac{\partial p_2}{\partial x} = 0 \end{aligned} \tag{94}$$

To enforce condition (93), an extra coefficient is added to the pressure equation of System (92):

$$\frac{1}{M^2} \frac{\partial p_0}{\partial t} + \rho_0 c_0^2 \frac{\partial u_0}{\partial x} = 0 \tag{95}$$

This penalization strategy, due to Turkel [43], forces solutions of System (92) to converge to incompressible solutions.

4.1.3 System considered for the Riemann problem

Inserting (95) in (92) and using (90 - 91), the following leading order system is obtained:

$$\begin{aligned} &\frac{\partial \rho}{\partial t} + u \frac{\partial \rho}{\partial x} + \rho \frac{\partial u}{\partial x} = 0 \\ &\frac{\partial u}{\partial t} + u \frac{\partial u}{\partial x} + \frac{1}{\rho} \frac{\partial p}{\partial x} = 0. \\ &\frac{\partial p}{\partial t} + M^2 u \frac{\partial p}{\partial x} + M^2 \rho c^2 \frac{\partial u}{\partial x} = 0 \end{aligned} \tag{96}$$

This system is hyperbolic and has the following wave speeds: $u, u + \tilde{c}_+, u - \tilde{c}_-$, with,

$$\tilde{c}_- = \frac{(1 - M^2)u + \sqrt{(M^2 - 1)^2 u^2 + 4M^2 c^2}}{2} \tag{97}$$

$$\tilde{c}_+ = \frac{(M^2-1)u + \sqrt{(M^2-1)^2u^2 + 4M^2c^2}}{2} \tag{98}$$

These wave speeds are directly used in the HLLC solver (136).
It is worth to mention that the Euler system is modified in the Riemann problem resolution only, where formulation (96) is used. With the fluxes computed with the HLLC solver, the Godunov method (135) is used with the conventional conservative formulation of the Euler equations and unmodified equation of state.
Thus, the flow model solved corresponds exactly to System (1) with the EOS (2). This method obviously guarantees conservation and correct jumps across waves. It only acts on the numerical dissipation.
As the conservative formulation is used, even strong discontinuities can be handled by the method. Also, as the Mach number can be chosen in (96), the method is able to compute fast flows. This remarkable feature has been observed and analyzed by Guillard and Viozat [12]. The validity and efficiency of this method is illustrated in Section 4 where comparisons with the exact solution are done, showing excellent agreement even when coarse meshes are used compared to the original Godunov method. We now address method extension to the two-phase flow model (3) and its pressure non equilibrium variant (5).

4.1.4 Two-phase low Mach preconditioning

The pressure non-equilibrium model (5) in primitive form reads:

$$\begin{aligned}
&\frac{\partial \alpha_1}{\partial t} + u\frac{\partial \alpha_1}{\partial x} = 0\\
&\frac{\partial \alpha_1\rho_1}{\partial t} + \alpha_1\rho_1\frac{\partial u}{\partial x} + u\frac{\partial \alpha_1\rho_1}{\partial x} = 0\\
&\frac{\partial \alpha_2\rho_2}{\partial t} + \alpha_2\rho_2\frac{\partial u}{\partial x} + u\frac{\partial \alpha_2\rho_2}{\partial x} = 0\\
&\frac{\partial u}{\partial t} + u\frac{\partial u}{\partial x} + \frac{1}{\rho}\frac{\partial P}{\partial x} = 0\\
&\frac{\partial e_1}{\partial t} + u\frac{\partial e_1}{\partial x} + \frac{p_1}{\rho_1}\frac{\partial u}{\partial x} = 0\\
&\frac{\partial e_2}{\partial t} + u\frac{\partial e_2}{\partial x} + \frac{p_2}{\rho_2}\frac{\partial u}{\partial x} = 0\\
&\frac{\partial P}{\partial t} + u\frac{\partial P}{\partial x} + \rho c^2\frac{\partial u}{\partial x} = 0
\end{aligned} \tag{99}$$

The pressure relaxation terms have been omitted as they are solved separately. This system admits the following frozen sound speed defined by:

$$c_f = \sqrt{Y_1c_1^2 + Y_2c_2^2} \tag{100}$$

This sound speed is very different from the mechanical equilibrium one given by (45). However, the equilibrium sound speed is recovered after the projection to pressure equilibrium summarized in Section 2.
As System (5) is overdetermined (see again Section 2 for details), its primitive variables formulation is also overdetermined. In particular, the mixture pressure equation and the two internal

energy equations form an overdetermined subsystem.
During low Mach preconditioning, in order to force the incompressibility condition,

$$\frac{\partial u}{\partial x} = 0, \tag{101}$$

when the Mach number tends to zero, the pressure equation has been modified with a penalization coefficient (Equation 95), resulting in System (96) in the single phase flows context. Here, the same preconditioned pressure formulation is adopted:

$$\frac{1}{M^2}\frac{\partial P}{\partial t} + u\frac{\partial P}{\partial x} + \rho c^2 \frac{\partial u}{\partial x} = 0 \tag{102}$$

Modifying the mixture pressure equation ($P = \alpha_1 p_1 + \alpha_2 p_2$) that appears in the momentum equation immediately modifies the wave speeds, as previously in the single phase flow case:

$$\tilde{c}_- = \frac{(1-M^2)u + \sqrt{(M^2-1)^2u^2 + 4M^2c_f^2}}{2} \tag{103}$$

$$\tilde{c}_+ = \frac{(M^2-1)u + \sqrt{(M^2-1)^2u^2 + 4M^2c_f^2}}{2} \tag{104}$$

Note that the Mach number that appears in the equations (103 - 104) is defined with the same sound speed (100). It means that, in the low Mach number limit, the following system is solved:

$$\begin{aligned}
&\frac{\partial \alpha_1}{\partial t} + u\frac{\partial \alpha_1}{\partial x} = 0,\\
&\frac{\partial \rho_1}{\partial t} + u\frac{\partial \rho_1}{\partial x} = 0,\\
&\frac{\partial \rho_2}{\partial t} + u\frac{\partial \rho_2}{\partial x} = 0,\\
&\frac{\partial u}{\partial t} + u\frac{\partial u}{\partial x} + \frac{1}{\rho}\frac{\partial P}{\partial x} = 0,\\
&\frac{\partial p_1}{\partial t} + u\frac{\partial p_1}{\partial x} = 0 \text{ or alternatively } \frac{\partial e_1}{\partial t} + u\frac{\partial e_1}{\partial x} = 0,\\
&\frac{\partial p_2}{\partial t} + u\frac{\partial p_2}{\partial x} = 0 \text{ or alternatively } \frac{\partial e_2}{\partial t} + u\frac{\partial e_2}{\partial x} = 0,\\
&\frac{\partial u}{\partial x} = 0
\end{aligned} \tag{105}$$

Knowledge of the limit internal energy equations will be of particular help for the low Mach Riemann solver presented hereafter.

Solving the Riemann problem Using the following notations :

$$Sl = u_l - \tilde{c_l} = u_l - \frac{(1-M^2)u_l + \sqrt{(M^2-1)^2u_l^2 + 4M^2c_l^2}}{2} \tag{106}$$

$$Sr = u_r + \tilde{c_r} = u_r + \frac{(M^2-1)u_r + \sqrt{(M^2-1)^2u_r^2 + 4M^2c_r^2}}{2} \tag{107}$$

And with HLL S_M approximation :

$$S_M = \frac{S_R(\rho u)_R - S_L(\rho u)_L - ((\rho u^2 + p)_R - (\rho u^2 + p)_L)}{S_R\rho_R - S_L\rho_L - ((\rho u)_R - (\rho u)_L)} \tag{108}$$

The corresponding Riemann problem can be represented as :

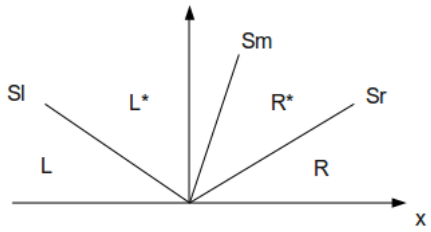

Figure 13: Description of the Riemann problem and associated wave speeds.

The Riemann problem is solved as explained in [38], except for the internal energy equations. The variables vector, U, and the flux vector, F, are defined as follows:

$$U = \begin{pmatrix} \alpha_1 \\ \alpha_1\rho_1 \\ \alpha_2\rho_2 \\ \alpha_1\rho_1 e_1 \\ \alpha_2\rho_2 e_2 \\ \rho u \\ \rho E \end{pmatrix} F = \begin{pmatrix} \alpha_1 u \\ \alpha_1\rho_1 u \\ \alpha_2\rho_2 u \\ \alpha_1\rho_1 e_1 u \\ \alpha_2\rho_2 e_2 u \\ \rho u^2 + P \\ (\rho E + P)u \end{pmatrix} \tag{109}$$

Using the low Mach number preconditioning leads to $\dfrac{\partial u}{\partial x} = 0$, which means that the internal energy equations can be re-written as:

$$\begin{aligned} \frac{\partial e_1}{\partial t} + u\frac{\partial e_1}{\partial x} &= 0 \\ \frac{\partial e_2}{\partial t} + u\frac{\partial e_2}{\partial x} &= 0 \end{aligned} \tag{110}$$

Therefore, there is no internal energy jump through the Sl and Sr waves.
Thus, the only modifications to the Riemann problem solving are the following:

$$\begin{aligned} e^*_{k,L} &= e_{k,L} \\ e^*_{k,R} &= e_{k,R} \end{aligned} \tag{111}$$

4.2 Preconditionned Riemann solvers illustrations

4.2.1 Single phase nozzle flow

The explicit Godunov scheme of Appendix 6 with HLLC Riemann solver is used, with the preconditioned wave speed (97 - 98) derived previously. The single phase Euler equations are first considered.

In the formulation (96), and consequently in the associated Riemann solver, given in Appendix

6, the Mach number M is set to a reference value M_{ref} which is used as constant in the entire flow field or variable at each cell boundary. To illustrate the method efficiency the same nozzle flow problem as studied previously in Figures (6 - 8) is considered.
A coarse mesh with 100 grid points is considered and the M_{ref} influence is studied. Corresponding results are shown in the Figures (14 - 15) at steady state.

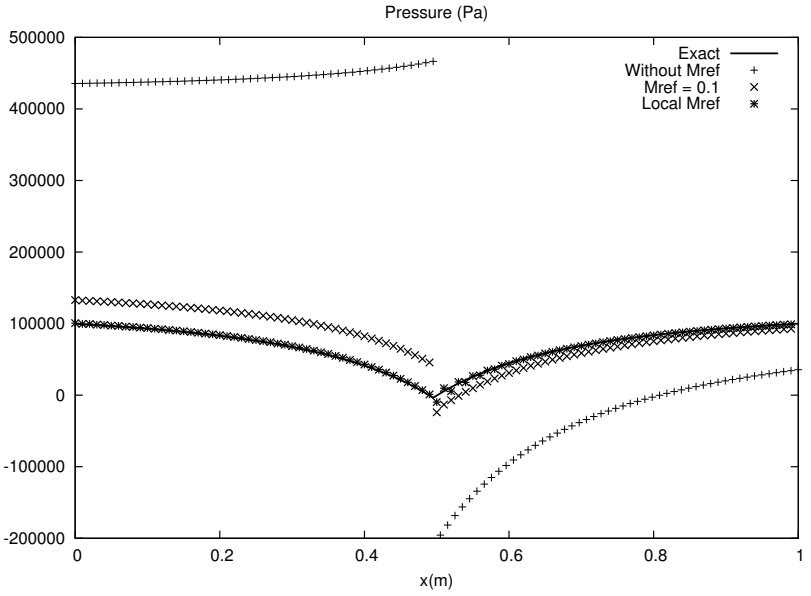

Figure 14: Computed pressure profiles in the Laval nozzle test with M_{ref}=0.1, M_{ref}=local Mach number and without M_{ref} are compared against the compressible exact solution. The error decreases dramatically as soon as M_{ref} is used and tends to the local Mach number.

4.2.2 Two phase nozzle flow

To illustrate the two-phase low Mach number preconditioning, the same nozzle flow problem as studied previously is considered. However, the liquid water at the inflow now contains a small fraction of air.
Mass flow rate and total enthalpy are imposed at left while the right outlet is opened to the atmosphere. The fluids used in the calculations correspond to liquid water and air, with the following SG EOS (2) parameters $\gamma_{water} = 4.4$, $P_{\infty,water} = 600MPa$, $\gamma_{air} = 1.4$, $P_{\infty,air} = 0Pa$. The imposed conditions at left are the following:

$$\begin{cases} m = 6500\, Kg.m^{-2}.s^{-1} \\ \rho_{water} = 1000\, Kg.m^{-3} \\ \rho_{air} = 1\, Kg.m^{-3} \\ \alpha_{water,0} = 0.9999 \\ P = 0.1\, MPa \end{cases}$$

The imposed total enthalpy is computed with $\rho_{water}, \rho_{air}, \alpha_{water,0}$ and P. With these boundary conditions, the numerical solution has been computed using different values of $M_{ref,min}$: 0.1,

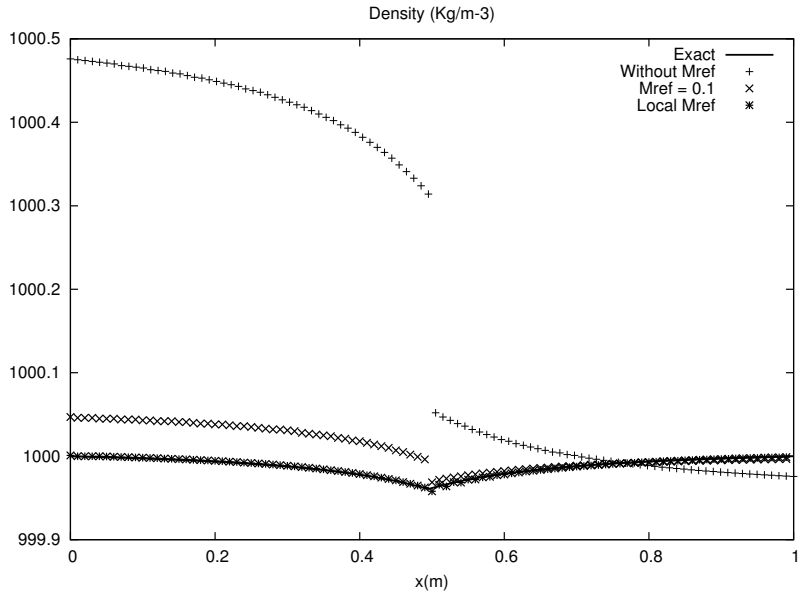

Figure 15: Computed density profiles in the Laval nozzle test with M_{ref}=0.1, M_{ref}=local Mach number and without M_{ref} are compared against the compressible exact solution. The error decreases dramatically as soon as M_{ref} is used and tends to the local Mach number.

0.05, 0.01 and two meshes containing 100 cells and 200 cells, respectively. $M_{ref,min}$ will be defined in the next subsection.

The following figures show clearly that the waves' speeds choice and the modification of the solver has dramatic consequences on method convergence in the low Mach number limit. It is also clear that the more M_{ref} tends to the true Mach number, in the low Mach limit, the better the solution is.

4.2.3 Preconditioning method precautions

It appears clearly that the waves' speeds choice in the HLLC solver has dramatic consequences on method convergence in the low Mach number limit. It is also clear that the more M_{ref} tends to the local Mach number, in the low Mach limit, the better the accuracy is. Therefore, the best solution consists in setting the reference Mach number, M_{ref}, to the local one, M_i. But, as the "sound speeds" (97 - 98) tend to wrong values when M tends to 0, the following function is used:

$$M^i_{ref} = \begin{cases} 1, \text{ if } M_i \geq 0.3 \\ M_i, \text{ if } 0.3 > M_i > M_{ref,min} \\ M_{ref,min}, \text{ if } M_i \leq M_{ref,min} \end{cases} \tag{112}$$

The minimum Mach number, $M_{ref,min}$ is typically 10^{-2} or 10^{-3}. The preconditioned sound speeds must be computed with a unique M^*_{ref} at a given cell boundary for the Riemann problem resolution:

$$M^*_{ref} = Max(M^L_{ref}, M^R_{ref}) \tag{113}$$

Where the superscripts "L" and "R" denote the left and right states of a cell boundary.
It is also important to report the computational cost to reach steady state on the previous

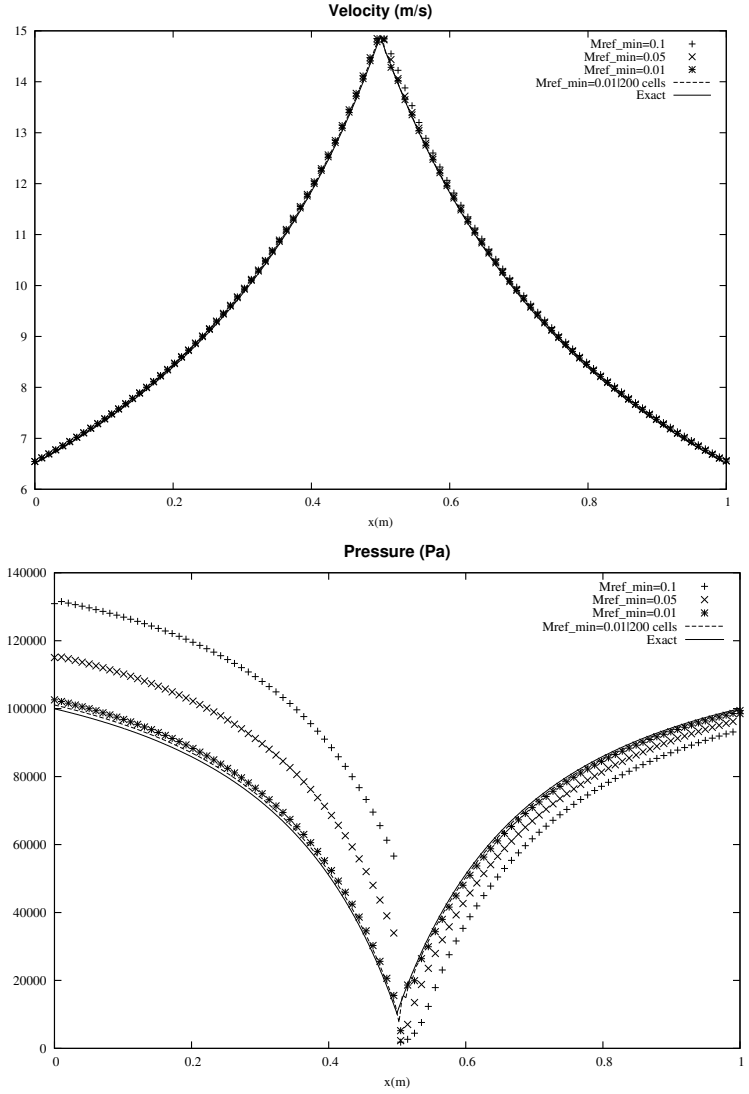

Figure 16: Computed mixture pressure and velocity profiles in the nozzle using different values of M_{ref} against the compressible exact solution. The error decreases dramatically as soon as M_{ref} is used and tends to the local Mach number.

computational example with this method . It is worth to mention that the stability restriction for such scheme is more restrictive than conventional CFL criterion for compressible flows. Indeed, the time step has to fulfill (Birken and Meister, 2005 [5]):

$$\Delta t \leq M_{ref} \frac{\Delta x}{Max(|u| + c)} \tag{114}$$

This explains the computational costs reported in the Tables (2 - 3):

The corresponding Godunov scheme with the low Mach preconditioning is thus accurate but still expensive due to the time step restriction (114). Is is thus mandatory to derive an implicit

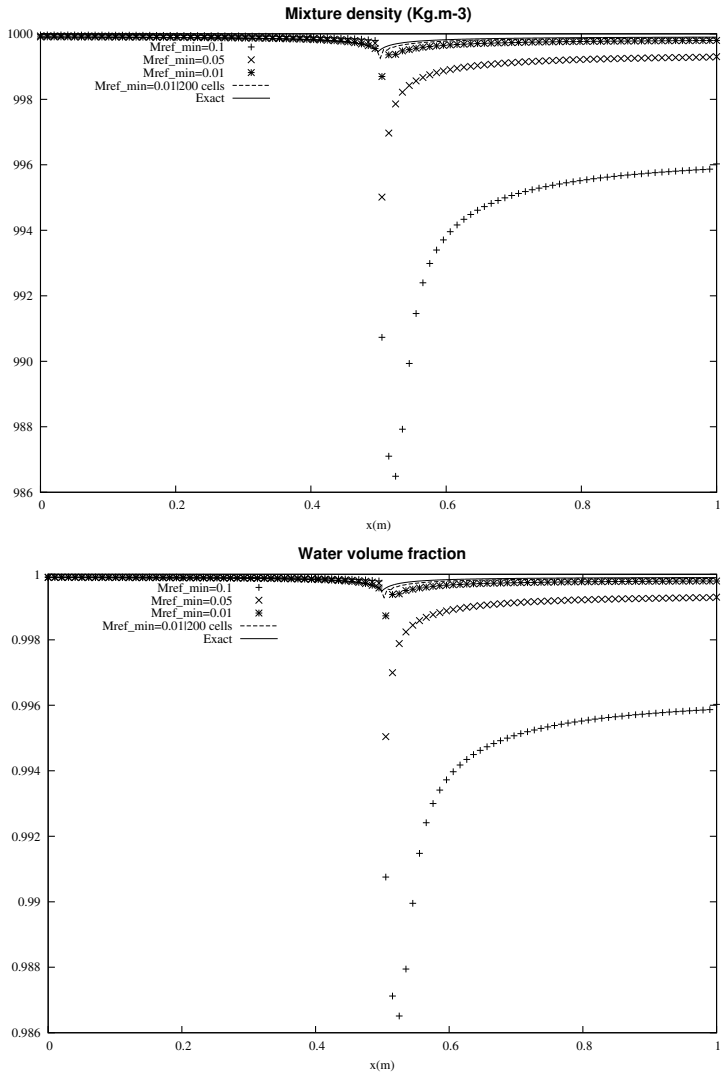

Figure 17: Computed mixture density and water volume fraction profiles in the nozzle using different values of M_{ref} against the compressible exact solution. The error decreases dramatically as soon as M_{ref} is used and tends to the local Mach number.

$M_{ref,min}$	CPU
0.1	3min 17s
Local Mach	1h 23min 12s

Table 2: Computational time versus M_{ref} for the Laval **single phase** nozzle test problem with 100 cells.

scheme.

$M_{ref,min}$	CPU
0.1	4min 06s
0.01	44min
0.01	2h 36min (200 cells)

Table 3: Computational time versus M_{ref} for the Laval **two-phase** nozzle test problem with 100 cells and 200 cells.

4.3 Implicit scheme for the Euler equations

As shown previously, the stability condition associated to preconditioned schemes is decreased by a factor proportional to the reference Mach number. It turns out that the resulting explicit schemes time steps are dramatically small. In order to overcome stability restrictions, an implicit scheme has to be used. For the sake of simplicity, the implicit scheme is first presented for the Euler equations in 1D. Multi-D and multiphase extensions will be addressed later.

4.3.1 Implicit Godunov scheme

On the basis of the explicit Godunov scheme (135), the implicit version reads:

$$U_i^{n+1} - U_i^n = -\frac{\Delta t}{\Delta x}(F_{i+\frac{1}{2}}^{n+1} - F_{i-\frac{1}{2}}^{n+1}) \tag{115}$$

Where the flux vectors $F_{i+\frac{1}{2}}^{n+1}$ and $F_{i-\frac{1}{2}}^{n+1}$ are computed according to variables at time t^{n+1}. Under Taylor expansion, the flux vectors become:

$$F_{i+\frac{1}{2}}^{n+1} = F_{i+\frac{1}{2}}^n + \frac{\partial F_{i+\frac{1}{2}}}{\partial U_i}\Big)^n (U_i^{n+1} - U_i^n) + \frac{\partial F_{i+\frac{1}{2}}}{\partial U_{i+1}}\Big)^n (U_{i+1}^{n+1} - U_{i+1}^n) \tag{116}$$

$$F_{i-\frac{1}{2}}^{n+1} = F_{i-\frac{1}{2}}^n + \frac{\partial F_{i-\frac{1}{2}}}{\partial U_i}\Big)^n (U_i^{n+1} - U_i^n) + \frac{\partial F_{i-\frac{1}{2}}}{\partial U_{i-1}}\Big)^n (U_{i-1}^{n+1} - U_{i-1}^n) \tag{117}$$

The flux appearing in these formulas, $F_{i+\frac{1}{2}}^n$, is solution of the Riemann problem and is consequently function of the left and right states: $F_{i+\frac{1}{2}}^n = F^*\left(U_i^n, U_{i+1}^n\right)$. The Riemann solver used here is the HLLC solver, already presented (136). Let's denote the variation:

$$\delta U_i = U_i^{n+1} - U_i^n \tag{118}$$

Rewriting Relations (115), (116) and (117) using (118), the following scheme is obtained:

$$\delta U_i \left[I + \frac{\Delta t}{\Delta x}\frac{\partial F_{i+\frac{1}{2}}}{\partial U_i}\Big)^n - \frac{\Delta t}{\Delta x}\frac{\partial F_{i-\frac{1}{2}}}{\partial U_i}\Big)^n \right] + \frac{\Delta t}{\Delta x}\frac{\partial F_{i+\frac{1}{2}}}{\partial U_{i+1}}\Big)^n \delta U_{i+1} - \frac{\Delta t}{\Delta x}\frac{\partial F_{i-\frac{1}{2}}}{\partial U_{i-1}}\Big)^n \delta U_{i-1} \tag{119}$$

$$= -\frac{\Delta t}{\Delta x}(F_{i+\frac{1}{2}}^n - F_{i-\frac{1}{2}}^n)$$

Under compact form it reads: $M\delta U = D$ with

$$M = \begin{Bmatrix} \mathrm{A} & \mathrm{C} & & & & (0) \\ \mathrm{B} & . & . & & & \\ & . & . & . & & \\ & & . & . & . & \\ & & & . & . & \mathrm{C} \\ (0) & & & & \mathrm{B} & \mathrm{A} \end{Bmatrix}, \delta U = \begin{bmatrix} \delta U_1 \\ . \\ . \\ . \\ \delta U_N \end{bmatrix}, D = \begin{bmatrix} . \\ . \\ -\frac{\Delta t}{\Delta x}(F_{i+\frac{1}{2}}^n - F_{i-\frac{1}{2}}^n) \\ . \\ . \end{bmatrix}$$

where the matrixes A, B and C are defined as follows:

$$\begin{cases} A = I_3 + \dfrac{\Delta t}{\Delta x}\left(\dfrac{\partial F_{i+\frac{1}{2}}}{\partial U_i}\right)^n - \dfrac{\Delta t}{\Delta x}\left(\dfrac{\partial F_{i-\frac{1}{2}}}{\partial U_i}\right)^n \\ B = -\dfrac{\Delta t}{\Delta x}\left(\dfrac{\partial F_{i-\frac{1}{2}}}{\partial U_{i-1}}\right)^n \\ C = \dfrac{\Delta t}{\Delta x}\left(\dfrac{\partial F_{i+\frac{1}{2}}}{\partial U_{i+1}}\right)^n \end{cases}$$

This tridiagonal system can be solved either by direct or by iterative methods. It is worth to mention that this method is a particular case of the Newton-Raphson method which can be presented as follows. Let's consider the function $G(\delta U)$ whose components are $G_i(\delta U) = \delta U + \dfrac{\Delta t}{\Delta x}(F^{n+1}_{i+\frac{1}{2}} - F^{n+1}_{i-\frac{1}{2}})$. The goal is to solve,

$$G(\delta U) = 0. \tag{120}$$

As $F^{n+1}_{i+\frac{1}{2}}$ and $F^{n+1}_{i-\frac{1}{2}}$ are non-linear functions of δU_i, one way to solve this equation is to use the Newton-Raphson metho, which, in this case, reads:

$$G(\delta U^{k+1}) = G(\delta U^k) + \left(\frac{\partial G(\delta U^k)}{\partial \delta U^k}\right)\left(\delta U^{k+1} - \delta U^k\right) \tag{121}$$

As the $G(\delta U^{k+1}) = 0$ condition has to be reached, the following formula is obtained:

$$\delta U^{k+1} = \delta U^k - \left[\left(\frac{\partial G(\delta U^k)}{\partial \delta U^k}\right)\right]^{-1} G(\delta U^k) \tag{122}$$

where δU^k represents δU at the k step of the iterative method. For practical applications, one or two iterations only are used. The present implicit Godunov type scheme needs an approximate Riemann solver to compute the numerical fluxes $F^n_{i\pm\frac{1}{2}}$ as well as the various flux derivatives.

4.3.2 Flux derivatives

As mentioned before, the HLLC flux (136), as many other Riemann solvers, can be formulated under the form:

$$F_{LR} = \frac{1}{2}\left(F_L + F_R\right) - \frac{1}{2}\sum_j^{n_w} sign(\lambda_j)\delta W_j \tag{123}$$

Where λ_j is the speed of the jth wave and δW_j is the associated variable jump across the corresponding wave.With these notations, the fluxes derivatives read:

$$\frac{\partial F_{LR}}{\partial U_L} = \frac{1}{2}\frac{\partial F_L}{\partial U_L} - \frac{1}{2}\sum_j^{n_w} sign(\lambda_j)\frac{\partial \delta W_j}{\partial U_L} \tag{124}$$

$$\frac{\partial F_{LR}}{\partial U_R} = \frac{1}{2}\frac{\partial F_R}{\partial U_R} - \frac{1}{2}\sum_j^{n_w} sign(\lambda_j)\frac{\partial \delta W_j}{\partial U_R} \tag{125}$$

The calculation details for the HLLC Riemann solver are given in the Appendix 6 .

4.3.3 Illustrations

To illustrate the implicit scheme efficiency, we consider the same test problem as before (Section 4.2.1).A coarse mesh with 100 grid points is considered. Corresponding results are shown in the Figures (18 - 19) at steady state. As expected, the implicit scheme is numerically stable for

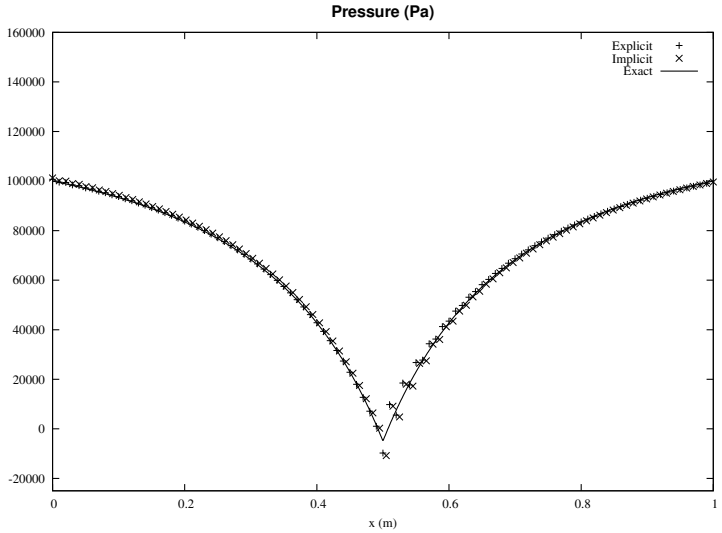

Figure 18: Computed pressure profiles in the Laval nozzle with $M_{ref} = M_i$ compared against the compressible exact solution. Implicit and explicit solutions show excellent agreement.

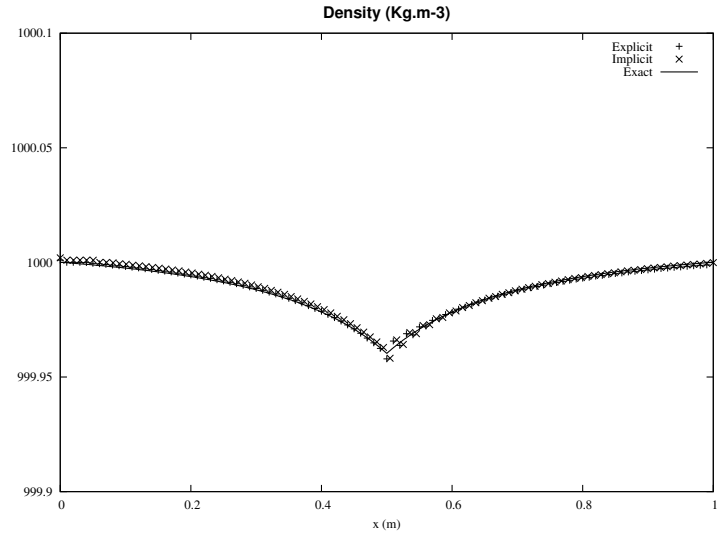

Figure 19: Computed density profiles in the Laval nozzle with $M_{ref} = M_i$ compared against the compressible exact solution. Implicit and explicit solutions show excellent agreement.

larger time steps. It is worth to mention that the computational time is now 4 min, with a CFL

coefficient equal to 0.15, to be compared to the computational time of 43 min needed by the explicit scheme, with a CFL coefficient equal to 0.0036 (As using the low Mach preconditioning with an explicit scheme requires the use of a time step reduced by a factor $M_{ref,min}$).

4.4 Multi-D extension

Multidimensional finite volume approximation is addressed. Let's consider a cell, i, and denote by $Vo(i)$ the set of neighbouring cells as shown in the Figure 20. Therefore, the implicit Godunov

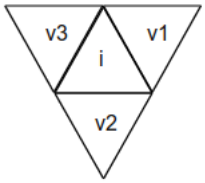

Figure 20: Schematic representation of a triangular cell with its set of neighbours, $Vo(i) = \{V_1, V_2, V_3\}$

finite volumes scheme reads:

$$(U_i^{n+1} - U_i^n) = -\frac{\Delta t}{V(i)} \sum_{j \in Vo(i)} F_{i,j}^{n+1} \tag{126}$$

Under similar notations as in 1D, the fluxes are expanded as follows:

$$F_{i,j}^{n+1} = F_{i,j}^n + \left(\frac{\partial F_{i,j}}{\partial U_i}\right)^n \left(U_i^{n+1} - U_i^n\right) + \left(\frac{\partial F_{i,j}}{\partial U_j}\right)^n \left(U_j^{n+1} - U_j^n\right) \tag{127}$$

Denoting the variation by $\delta U_i = U_i^{n+1} - U_i^n$ and using (127) in (126) the following scheme is obtained:

$$\left(I + \frac{\Delta t}{V(i)} \sum_{j \in Vo(i)} A_{ii}^j\right) \delta U_i + \frac{\Delta t}{V(i)} \sum_{j \in Vo(i)} \left(A_{ij}^j \delta U_j\right) = -\frac{\Delta t}{V(i)} \sum_{j \in Vo(i)} F_{i,j}^{n+1} \tag{128}$$

with

$$\begin{cases} A_{ii}^j = \left(\dfrac{\partial F_{i,j}}{\partial U_i}\right)^n \\ A_{ij}^j = \left(\dfrac{\partial F_{i,j}}{\partial U_j}\right)^n \end{cases}$$

Under compact form it reads:

$$M \delta U = D$$

where

$$\delta U = \begin{bmatrix} \delta U_1 \\ . \\ . \\ . \\ \delta U_N \end{bmatrix}, D = \begin{bmatrix} . \\ . \\ -\dfrac{\Delta t}{V(i)} \sum_{j \in Vo(i)} F_{i,j}^{n+1} S(ij) \\ . \\ . \end{bmatrix}$$

The M matrix shape depends on the number of faces per cell. In order to lower the computational time, the sparse character of the M matrix has to be exploited. In this paper, we chose to use the CSC (Compressed Sparse Column) method, which is well explained in the book [33]. Method's accuracy can be improved by using higher order extension, as detailed in the Appendix 6 .

4.5 Implicit scheme for the two-phase flow model

In this section, the implicit scheme for the hyperbolic two-phase flow model is addressed. The model corresponds to System (5) without relaxation terms. These equations can be arranged in two sets: Conservative equations on one hand and non-conservatives equations on the other hand. The conservative set of equations reads:

$$\frac{\partial \Omega}{\partial t} + \frac{\partial F(U)}{\partial x} = 0 \tag{129}$$

The non-conservative set of equations reads:

$$\frac{\partial V}{\partial t} + \frac{\partial G(U)}{\partial x} + H(U)\frac{\partial u}{\partial x} = 0 \tag{130}$$

Where :

$$U = \begin{pmatrix} \Omega \\ V \end{pmatrix}, \Omega = \begin{pmatrix} \alpha_1\rho_1 \\ \alpha_1\rho_2 \\ \rho\mathbf{u} \\ \rho E \end{pmatrix}, V = \begin{pmatrix} \alpha_1 \\ \alpha_1\rho_1 e_1 \\ \alpha_2\rho_2 e_2 \end{pmatrix} \tag{131}$$

and

$$F(U) = \begin{pmatrix} \alpha_1\rho_1\mathbf{u} \\ \alpha_1\rho_2\mathbf{u} \\ \rho\mathbf{u}^2 + P \\ (\rho E + P)\mathbf{u} \end{pmatrix} G(U) = \begin{pmatrix} \alpha_1\mathbf{u} \\ \alpha_1\rho_1 e_1\mathbf{u} \\ \alpha_2\rho_2 e_2\mathbf{u} \end{pmatrix} H(U) = \begin{pmatrix} -\alpha_1 \\ \alpha_1 p_1 \\ \alpha_2 p_2 \end{pmatrix} \tag{132}$$

The implicit scheme derived previously for the Euler equations can be used for the conservative equations System with some modifications. Indeed, the pressure, P, and the mixture total energy, E, are now function of $\rho, e, \alpha_1, \alpha_2$ (6). Therefore, the derivatives involved in the implicit flux computation are more complex. Their expressions are given in Appendix 6. Most of the efforts are focused on the implicit scheme for the non-conservative equations System. Approximating (130) implicitly reads:

$$V_i^{n+1} = V_i^n - \frac{\Delta t}{\Delta x}\left(G_{i+\frac{1}{2}}^{*,n+1} - G_{i-\frac{1}{2}}^{*,n+1} + H(U)_i^{n+1}\left(u_{i+\frac{1}{2}}^{*,n+1} - u_{i-\frac{1}{2}}^{*,n+1}\right)\right) \tag{133}$$

Using the same development as previously (116 - 117), the following scheme is obtained:

$$\begin{aligned} &\left[I + \frac{\Delta t}{\Delta x}\left(\frac{\partial G_{i+\frac{1}{2}}^n}{\partial U_i} - \frac{\partial G_{i-\frac{1}{2}}^n}{\partial U_i} + H_i^n\left[\frac{\partial u_{i+\frac{1}{2}}^*}{\partial U_i} - \frac{\partial u_{i-\frac{1}{2}}^*}{\partial U_i}\right] + (u_{i+\frac{1}{2}}^* - u_{i-\frac{1}{2}}^*)\frac{\partial H_i^n}{\partial U_i}\right)\right]\delta V_i \\ &+ \frac{\Delta t}{\Delta x}\left[\frac{\partial G_{i+\frac{1}{2}}}{\partial U_{i+1}} + H_i^n\frac{\partial u_{i+\frac{1}{2}}^*}{\partial U_{i+1}}\right]\delta V_{i+1} - \frac{\Delta t}{\Delta x}\left[\frac{\partial G_{i-\frac{1}{2}}}{\partial U_{i-1}} + H_i^n\frac{\partial u_{i-\frac{1}{2}}^*}{\partial U_{i-1}}\right]\delta V_{i-1} \\ &= -\frac{\Delta t}{\Delta x}\left(G_{i+\frac{1}{2}}^{*,n} - G_{i-\frac{1}{2}}^{*,n} + H_i^n\left(u_{i+\frac{1}{2}}^{*,n} - u_{i-\frac{1}{2}}^{*,n}\right)\right) \end{aligned} \tag{134}$$

The various expressions for the derivatives are detailed in Appendix 6.

5 Illustrations and validations

5.1 One dimensional two-phase nozzle flow

To illustrate the performance of the two phase implicit scheme, we consider the same two-phase nozzle flow test as before (Section 4.2.2).The numerical solution has been computed using different values of $M_{ref,min}$(0.1 and 0.01) as well as two different meshes (100 and 200 cells). Corresponding results are shown in the Figures (21 - 22) at steady state. The implicit scheme

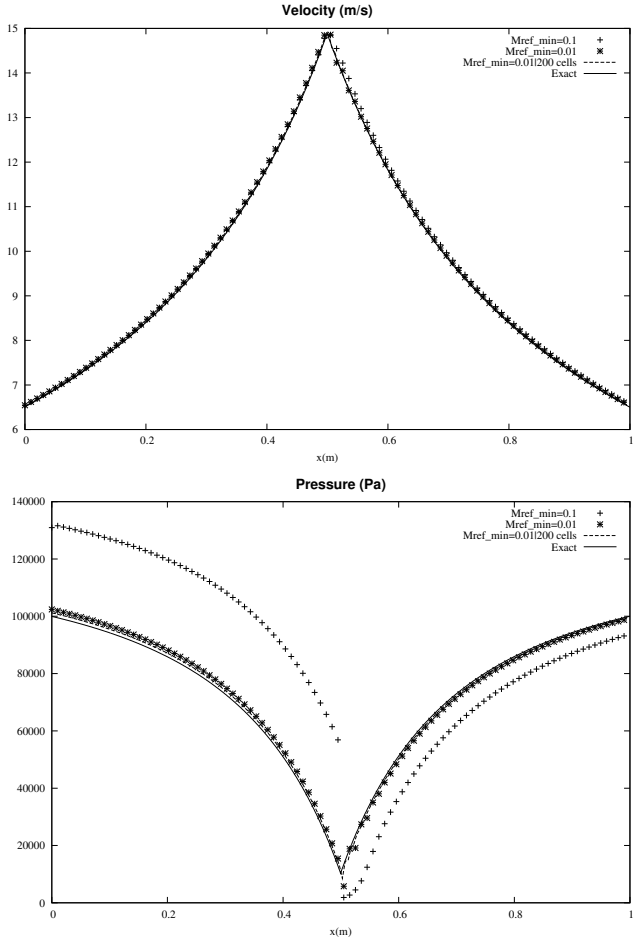

Figure 21: Computed mixture pressure and velocity profiles in the nozzle using different values of $M_{ref,min}$ against the compressible exact solution. The error decreases dramatically as soon as M_{ref} is used. The exact solution is reached when $M_{ref,min}$ is equal to the local Mach minimum (0.01).

has presented the same behaviour and accuracy as the explicit version. The corresponding computational cost is reported in the Table 4. Compared to the explicit calculation times (Table 3), considerable saving appear as the implicit scheme reduces the computation times by a factor 18. To conclude, the implicit scheme presented in the previous section is efficient and accurate for two-phase flow calculations. Multi-D two-phase examples are addressed in the next paragraph.

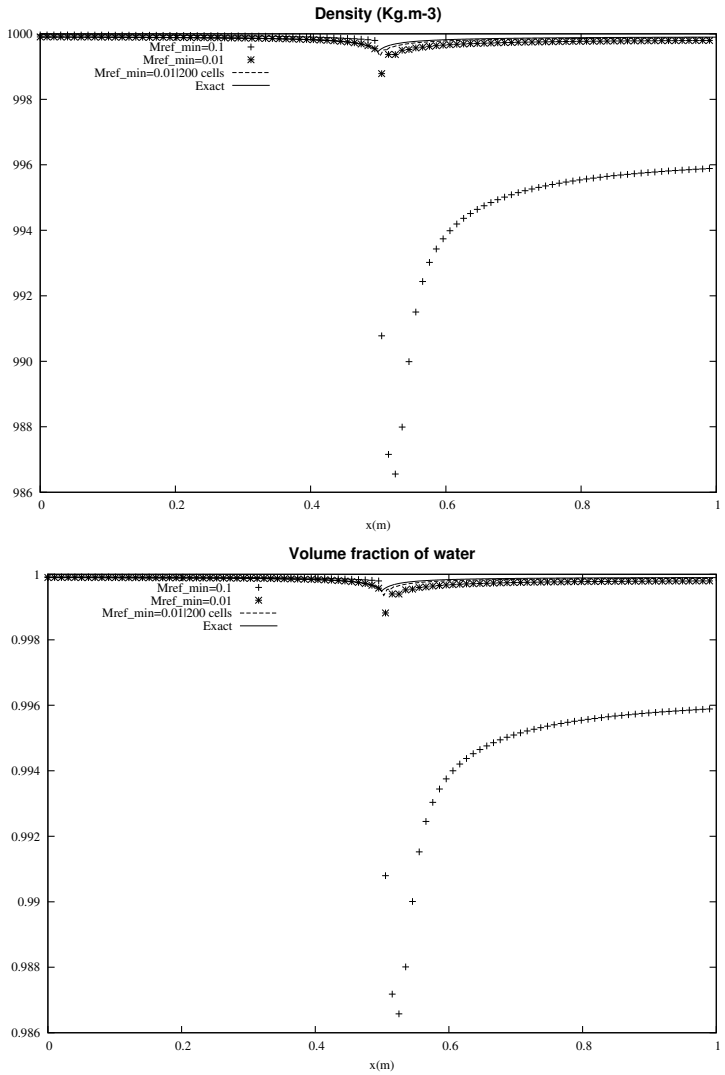

Figure 22: Computed mixture pressure and water volume fraction profiles in the nozzle using different values of $M_{ref,min}$ against the compressible exact solution. The error decreases dramatically as soon as M_{ref}. The exact solution is reach when $M_{ref,min}$ is equal to the local Mach minimum (0.01).

$M_{ref,min}$	CPU	Implicit CFL	Explicit CFL
0.1	46s	3.0	0.09
0.01	8min 45s (200 cells)	1.5	0.009

Table 4: Computational time versus M_{ref} for the Laval **two phase** nozzle test problem with the implicit scheme.

5.2 3D Computations of cavitating flows in Venturi channels

In this paragraph, a 3D two phase nozzle flow case is addressed. We first present the geometry and the test parameters. Then, numerical results are compared against the experimental records.

5.2.1 Test case presentation

The experimental facility has been built at LEGI Laboratory, Grenoble, France by the group leaded by S. Barre. The test section corresponds to a Venturi channel with a nozzle divergent inclined at an angle of 8°. The geometry is shown in the Figure 23: The corresponding point

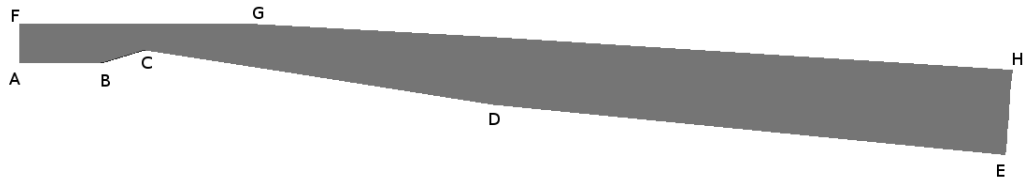

Figure 23: LEGI 8° Venturi geometry

coordinates are given in the Table 5 : As phase transition occurs at the throat, heat and mass

	X (abscissa) (m)	Y (m)		X(abscissa) (m)	Y (m)
A	0	0	E	1.225	-0.114
B	0.1	0	F	0	0.0488
C	0.153	0.0157	G	0.271	0.0488
D	0.588	-0.0517	H	1.233	-0.00845

Table 5: Venturi 8° points coordinates.

transfer have to be considered. These effects are accounted for by considering extra relaxation effects in addition to pressure relaxation. Indeed, as detailed in Saurel et al. [39], temperature and Gibbs free energy relaxation have to be considered. Appropriate relaxation solver is summarized in the appendix 6. Simulating phase transition requires appropriate EOS parameters. The fluids considered correspond to liquid water and water vapor, with the following SG EOS (2) parameters $\gamma_{liq} = 1.234$, $P_{\infty,liq} = 2532.302\,Atm$, $\gamma_{vap} = 1.316$ and $P_{\infty,air} = 0\,Pa$. These parameters have been computed following the method detailed in [27].

Inflow mass flow rate and total enthalpy are imposed and a prescribed pressure is imposed at the outlet. The imposed conditions at the left inflow entrance are the following,

$$\begin{cases} m = 7514.917\,Kg.m^{-2}.s^{-1} \\ \rho_{liq} = 1067.566\,Kg.m^{-3} \\ \rho_{vap} = 0.387\,Kg.m^{-3} \\ \alpha_{liq} = 0.999 \\ P = 51825\,Pa \end{cases}$$

while, at the right outlet, the prescribed pressure is $P = 72025Pa$.

5.2.2 Experimental results

The 8° Venturi channel of Figure 23 has been used at LEGI(Grenoble, France) to create cavitating glows. With the boundary conditions reported in the previous paragraph, a periodic flow is observed, as shown in the Fig 24. In the first stage of the cycle (a), a cavitation sheet is attached

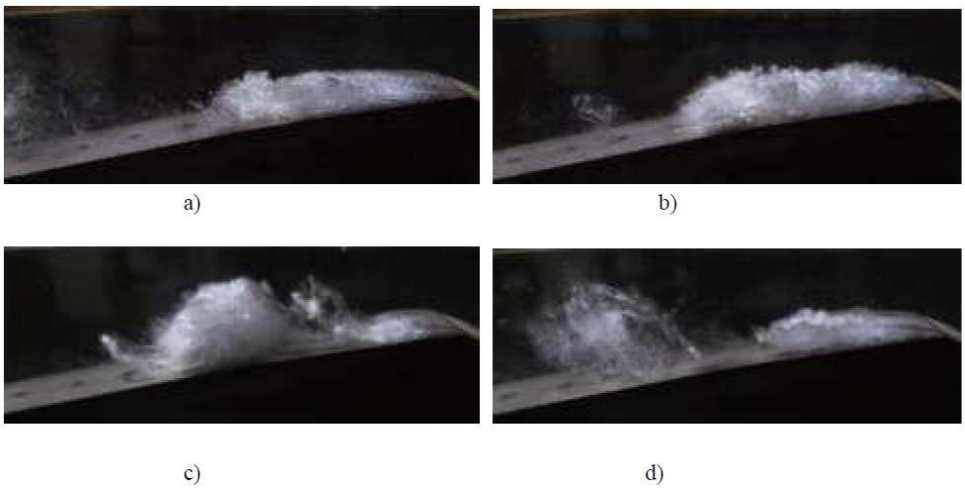

Figure 24: Instantaneous pictures of a break off cycle. Courtesy of S.Barre, LEGI, Grenoble, France.

to the throat and grows. In a second stage, the sheet reaches its maximum length (b) and breaks in two parts (c). At the end, the downstream part is swept along within the stream and starts to collapse while the attached part starts another cycle (d). The mean attached cavity length value is 45 $\pm$ 5 mm while the quasi-periodic vapor clouds shedding frequency is about 45 Hz. It is worth to mention that the cloud shedding frequency was calculated using spectral analysis of pressure measurement in the Venturi divergent.

5.2.3 Numerical results

A 3D unstructured mesh contain 52450 cells is used (Fig. 25). The grid is refined at the throat in order to capture the cavitation pocket. The average cell size is 0.013 mm at the throat and 0.08 mm elsewhere. As a Venturi geometry is 2D, there is only one cell in the z-direction. Using this mesh with the two-phase 3D implicit scheme along with the two phase low Mach preconditioning ($M_{ref,min}$ is set to 0.04) on a cluster with 24 CPU, allowed to reach 1.8s of physical time in about 97h with an average CFL coefficient equals to 28. This physical time was long enough to obtain a quasi-stationary flow with quasi-periodic vapor clouds shedding. An example of the obtained cloud shedding is shown in the volume fraction contours of Figure 26. A pressure signal is also recorded using a numerical jauge located in the middle of the $\overline{EH}$ segment, at the end of the Venturi divergent (Fig. 23). Using the water vapor volume fraction, we were able to determine a vapor clouds shedding frequency of about 43Hz. In order to verify this observed frequency, a spectral analysis of the recorded pressure signal was performed. The obtained spectrum is shown in the Figure. 27. The maximum intensity is reach for frequencies between 40 and 50Hz, which is in excellent agreement with the observed clouds shedding frequency. By performing measurements during every cycle, an average attached cavity length of about 45 mm has been measured from the computations. This results show remarkable agreement with the experiments.

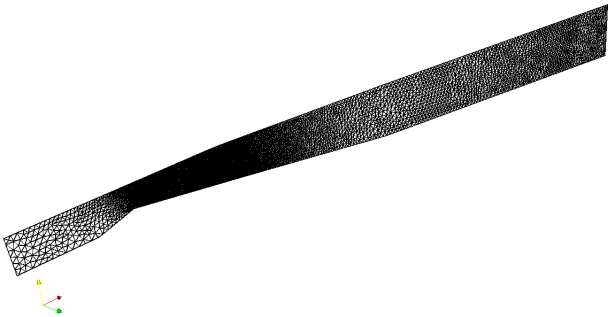

Figure 25: Venturi 8° 3D unstructured mesh.

Indeed, experimental measurements give a mean attached cavity length equals to 45 ± 5 mm.

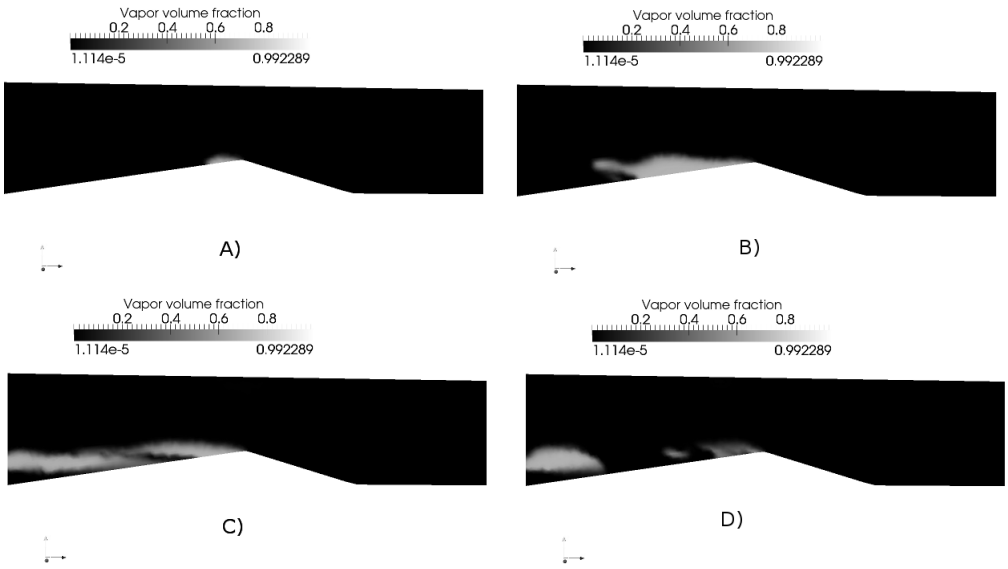

Figure 26: Computed volume fraction of water vapor. This example of the computed break off cycles shows the same four different parts as those observed during the experimental studies and shown in the Figure 24. The mean attached cavity length is about 45mm, in perfect agreement with the experiments.

These results prove that, contrarily to preceding conclusions of Coutier-Delgosha et al. [28], the effects of turbulence modeling is negligible in this kind of nozzle flow, as perfect agreement is reached, provided that:

- The model is in agreement with the fundamental principles of total energy conservation and entropy inequality.
- The algorithm is suited for two-phase all Mach number conditions.

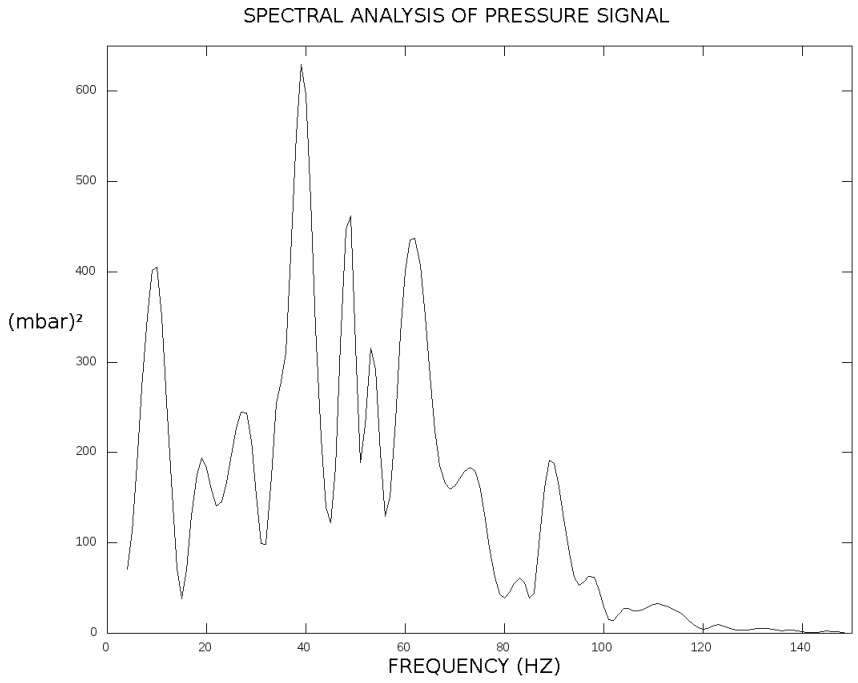

Figure 27: Spectral analysis of the recorded pressure signal using a pressure jauge located at the end of the Venturi divergent. The obtained spectrum shows maximum intensity for frequencies between 40 and 50 Hz. This is in excellent agreement with the observed cloud shedding frequency of 43Hz and in excellent agreement with the experimental frequency of 45 ± 5 Hz.

6 Conclusion

The design of accurate numerical schemes require reference solutions. In the present paper, single phase and two-phase quasi one-dimensional steady state solutions have been obtained. They have been widely used to check the accuracy of preconditioned numerical schemes. The Turkel preconditioned formulation has been used in the Riemann problem solution determination and embedded in the Godunov method with HLLC scheme, in both explicit and implicit versions. This variant of the Turkel method, due to Guillard and Viozat [13], has shown particular efficiency for all Mach number single phase flow conditions. It has been extended to the two-phase flow model of Kapila et al [19], particularly suited for interfacial flows [38] as well as cavitating flows [39]. Compared to conventional cavitation model widely used in industry, this model is not barotropic as it conserves energy. Also, phase transition is modeled in a thermodynamically consistent way.

The preconditioning method requires mild modifications on the internal energy jumps conditions in the Riemann problem that have important consequences on method convergence. The method has been validated against exact 1D solutions and experimental 2D cavitating Venturi flows. Without using any adjustable parameter, perfect agreement has been obtained, contrarily to previous attempts.

References

[1] R. Abgrall. How to prevent pressure oscillations in multicomponent flow calculations: A quasi conservative approach. *Journal of Computational Physics*, 125:150–160, (1996).

[2] T. Alazard. Low Mach number limit of the full Navier-Stokes equations. *Arch. Ration. Mech. Anal.*, 180(1):1–73, (2006).

[3] D.P. Babii, S.K.Godunov, V.T. Zhukov, and O.B. Feodoritova. On the different approximations of overdetermined hyperbolic equations of classical mathematical physics. *Comp. Mathematics and Mathematics Physics*, 47(3):427–441, (2007).

[4] T.J. Barth and D.C. Jespersten. The design and application of upwind schemes on unstructured meshes. *Proceedings of the AIAA 27th Aerospace Sciences Meeting (Reno, Nevada)*, (1989).

[5] P. Birken and A. Meister. On low Mach number preconditioning of finite volume schemes. *Proc. Appl. Math. Mech.*, 5:759–760, (2005).

[6] B. Braconnier and B. Nkonga. An all-speed relaxation scheme for interface flows with surface tension. *Journal of Computational Physics*, 228(16):5722 – 5739, (2009).

[7] S.F. Davis. Simplified second-order Godunov-type methods. *SIAM J. Sci. Statist. Comput.*, 9:445–473, (1988).

[8] D. G. Ebin. The motion of slightly compressible fluids viewed as a motion with strong constraining force. *Ann. of Math*, 105(1):141–200, (1977).

[9] N. Favrie, S.L. Gavrilyuk, and R. Saurel. Solid-fluid diffuse interface model in cases of extreme deformations. *Journal of Computational Physics*, 228(16):6037 – 6077, (2009).

[10] R. Fedkiw, Aslam T., Merriman B., and Osher S. A non-oscillatory Eulerian approach to interfaces in multimaterial flows (the Ghost Fluid Method). *Journal of Computational Physics*, 152(2):457–492, (1999).

[11] J. Glimm, J.W. Grove, X.L. Li, K.M. Shyue, Q. Zhang, and Y. Zeng. Three dimensional front tracking. *SIAM J. Scientific Computing*, 19:703–727, (1998).

[12] H. Guillard and C. Viozat. On the behaviour of upwind schemes in the low mach number limit. *Computers and Fluids*, 28:63–86, (1999).

[13] H. Guillard and C. Viozat. On the behaviour of upwind schemes in the low mach number limit. *Computers and Fluids*, 28(1):63 – 86, (1999).

[14] F. Harlow and A. Amsden. Fluid dynamics. *Monograph LA, Los Alamos National Laboratory, Los Alamos,NM*, LA-4700:1678–1712, (1971).

[15] F. Harlow and A. Amsden. A numerical fluid dynamics calculation method for all flow speeds. *Journal of Computational Physics*, 8(2):197 – 213, (1971).

[16] A. Harten, P.D. Lax, and B. van Leer. On upstream differencing and Godunov-type schemes for hyperbolic conservation laws. *SIAM Rev.*, 25:35–61, (1983).

[17] C.W. Hirt and B.D. Nichols. Volume of fluid (VOF) method for the dynamics of free boundaries. *Journal of Computational Physics*, 3:201–255, (1981).

[18] D. Juric and G. Tryggvason. Computations of boiling flows. *International Journal of Multiphase Flow*, 24(3):387 – 410, (1998).

[19] A.K. Kapila, R. Menikoff, J.B. Bdzil, S.F. Son, and D.S. Stewart. Two-phase modeling of of deflagration-to-detonation transistion in granular materials: Reduced equations. *Physics of Fluids*, 13:3002–3024, (2001).

[20] S. Klainerman and A. Majda. Singular limits of quasilinear hyperbolic systems with large parameters and the incompressible limit of compressible fluids. *Comm. Pure Appl. Math*, 34(4):481–524, (1981).

[21] S. Kokh and F. Lagoutière. An anti-diffusive numerical scheme for the simulation of interfaces between compressible fluids by means of a five-equation model. *Journal of Computational Physics*, 229(8):2773 – 2809, (2010).

[22] B. Lafaurie, C.Nardone, R. Scardovelli, S. Zaleski, and G. Zanetti. Modelling merging and fragmentation in multiphase flows with SURFER. *Journal of Computational Physics*, 113:134–147, (1994).

[23] DJ. Mavripilis. Revisiting the least-squares procedure for gradient reconstruction on unstructured meshes. *AIAA 16th Computational Fluid Dynamics Conference*, page 3986, (2003).

[24] T. Menard, S. Tanguy, and A. Berlemont. Coupling Level Set/VOF/Ghost Fluid methods. Validations and application to 3D simulation of the primary break-up of a liquid jet. *Int. J. of Multiphase Flow*, 33(5):510–524, (2007).

[25] R. Menikoff and B.J. Plohr. The Riemann problem for fluid flow of real materials. *Rev. Mod. Phys.*, 61:75–130, (1989).

[26] G. Metivier and S. Schochet. The incompressible limit of the non-isentropic Euler equations. *Arch. Ration. Mech. Anal.*, 158(1):61–90, (2001).

[27] O. Le Métayer, J. Massoni, and R. Saurel. Élaboration des lois d'état d'un liquide et de sa vapeur pour les modèles d'écoulements diphasiques. *International Journal of Thermal Sciences*, 43(3):265 – 276, (2004 (in French)).

[28] R. Fortes-Patella O. Coutier-Delgosha and J.L. Rebond. Evaluation of the turbulence model influence on the numerical simulations of unsteady cavitation. *J. Fluid Engineering*, 125(1):38–45, (2003).

[29] G. Perigaud and R. Saurel. A compressible flow model with capillary effects. *Journal of Computational Physics*, 209:139–178, (2005).

[30] F. Petitpas, E. Franquet, R. Saurel, and O. Le Metayer. A relaxation-projection method for compressible flows. Part II: Artificial heat exchanges for multiphase shocks. *Journal of Computational Physics*, 225(2):2214 – 2248, (2007).

[31] F. Petitpas, J. Massoni, R. Saurel, E. Lapebie, and L. Munier. Diffuse interface model for high speed cavitating underwater systems. *International Journal of Multiphase Flow*, 35(8):747 – 759, (2009).

[32] F. Petitpas, R. Saurel, E. Franquet, and A. Chinnayya. Modelling detonation waves in condensed energetic materials : Multiphase CJ conditions and multidimensionnal computations. *Shock Waves*, 19:377–401, (2009).

[33] Y. Saad. Numerical methods for large eigenvalue problems. *Manchester University Press*, (1992).

[34] R. Saurel and R. Abgrall. A multiphase Godunov method for multifluid and multiphase flows. *Journal of Computational Physics*, 150:425–467, (1999).

[35] R. Saurel, E. Franquet, E. Daniel, and O. Le Metayer. A relaxation-projection method for compressible flows. Part I: The numerical equation of state for the Euler equations. *Journal of Computational Physics*, 223(2):822 – 845, (2007).

[36] R. Saurel, O. Le Metayer, J. Massoni, and S. Gavrilyuk. Shock jump relations for multiphase mixtures with stiff mechanical relaxation. *Shock Waves*, 16:209–232, (2007).

[37] R. Saurel, N.Favrie, F.Petitpas, M-H.Lallemand, and S.L. Gavrilyuk. Modelling dynamic and irreversible powder compaction. *Journal of Fluid Mechanics*, 664:348–396, (2010).

[38] R. Saurel, F. Petitpas, and R. A.Berry. Simple and efficient methods relaxation for interfaces separating compressible fluids, cavitating flows and shocks in multiphase mixtures. *J. Comput. Phys.*, 228:1678–1712, (2009).

[39] R. Saurel, F. Petitpas, and R. Abgrall. Modelling phase transition in metastable liquids: Application to cavitating and flashing flows. *Journal of Fluid Mechanics*, 607:313–350, (2008).

[40] S. Schochet. The compressible Euler equations in a bounded domain: Existence of solutions and the incompressible limit. *Comm. Math. Phys.*, 104(1):49–75, (1986).

[41] R. Shukla, C. Pantano, and J. Freund. An interface capturing method for the simulation of multi-phase compressible flows. *Journal of Computational Physics*, 229(19):7411 – 7439, (2010).

[42] E.F. Toro, M. Spruce, and W. Speares. Restoration of the contact surface in the HLL-Riemann solver. *Shock Waves J.*, 4:25–34, (1994).

[43] E. Turkel. Preconditioned methods for solving the incompressible and low speed compressible equations. *Journal of Computational Physics*, 72(2):277 – 298, (1987).

[44] B. Van Leer. Towards the ultimate conservative difference scheme, V.A second order sequel to Godunov's method. *J. Comput. Phys.*, 32:445–473, (1979).

[45] A.B. Wood. A textbook of sound. *Bell Eds*, (1930).

Appendix A -Godunov HLLC scheme for the Euler equations in ducts of smooth varying cross sections

Consider a computational cell corresponding to an arbitrary control volume of the nozzle, as show in the Figure 28 :

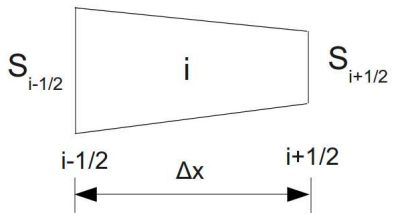

Figure 28: A computational cell i with its two cell boundaries, i+1/2 and i-1/2.

The conventional 1D Godunov scheme for ducts of smooth varying cross sections reads :

$$U_i^{n+1} = U_i^n - \frac{\Delta t}{V_i}\left(F^*_{i+\frac{1}{2}} S_{i+\frac{1}{2}} - F^*_{i-\frac{1}{2}} S_{i-\frac{1}{2}}\right) + \frac{\Delta t}{V_i} G_i \left(S_{i+\frac{1}{2}} - S_{i-\frac{1}{2}}\right) \tag{135}$$

with

$$U = \begin{pmatrix} \rho \\ \rho u \\ \rho E \end{pmatrix} \quad F = \begin{pmatrix} \rho u \\ \rho u^2 + p \\ (\rho E + p)u \end{pmatrix} \quad G_i = \begin{pmatrix} 0 \\ p_i^n \\ 0 \end{pmatrix}$$

Where :
- U represents the conservative variables vector,
- F represents the flux vector,
- S represents the cell boundary surface,
- V_i represents the cell volume .

The HLLC Riemann solver (Toro et al.) [42] is used to compute the intercell flux F^*. At cell boundary $i + \frac{1}{2}$, it reads:

$$F_{L,R} = \frac{1}{2}(F_L + F_R) - sign(S_L)\frac{S_L}{2}(U_L^* - U_L) - sign(S_M)\frac{S_M}{2}(U_R^* - U_L^*) - sign(S_R)\frac{S_R}{2}(U_R - U_R^*) \tag{136}$$

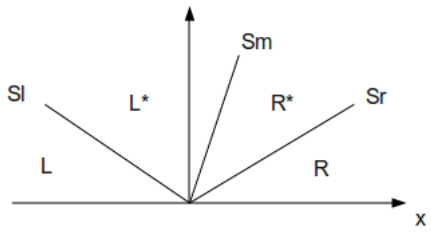

Figure 29: Schematization of the Euler equations Riemann problem under HLL approximation and associated wave speeds.

The subscripts L and R denote the left and right state of the Riemann problem, respectively. The wave speeds S_R and S_L are estimated with Davis approximation [7],

$$S_R = Max(u_R + c_R, u_L + c_L) \tag{137}$$

$$S_L = Max(u_R - c_R, u_L - c_L) \tag{138}$$

while S_M is estimated under HLL [16] approximation :

$$S_M = \frac{S_R U_R(2) - S_L U_L(2) - (F_R(2) - F_L(2))}{S_R U_R(1) - S_L U_L(1) - (F_R(1) - F_L(1))} \tag{139}$$

The states U_L^* and U_R^* are determined with the help of Rankine-Hugoniot jump relations across the S_R and S_L waves,

$$F_L^* - S_L U_L^* = F_L - S_L U_L, \tag{140}$$

$$F_R^* - S_R U_R^* = F_R - S_R U_R, \tag{141}$$

and continuity relations : $u_L^* = u_R^* = SM$ and $p_L^* = p_R^* = p^*$:

$$U_L^* = \frac{1}{S_M - S_L}[F_L - S_L U_L - (0, p^*, S_M.p^*)^T] \tag{142}$$

$$U_R^* = \frac{1}{S_M - S_R}[F_R - S_R U_R - (0, p^*, S_M.p^*)^T] \tag{143}$$

Appendix B -HLLC Riemann solver derivatives

The HLLC approximate Riemann solver is recalled hereafter:

$$F_{L,R} = \frac{1}{2}(F_L + F_R) - sign(S_L)\frac{S_L}{2}(U_L^* - U_L) - sign(S_M)\frac{S_M}{2}(U_R^* - U_L^*) - sign(S_R)\frac{S_R}{2}(U_R - U_R^*),$$

The flux vector derivatives are given by:

$$\frac{\partial F_{LR}}{\partial U_L} = \frac{1}{2}\frac{\partial F_L}{\partial U_L} - sign(S_L)\frac{S_L}{2}(\frac{\partial U_L^*}{\partial U_L} - 1) - sign(S_M)\frac{S_M}{2}(\frac{\partial (U_R^* - U_L^*)}{\partial U_L}) + sign(S_R)\frac{S_R}{2}(\frac{\partial U_R^*}{\partial U_L}) \tag{144}$$

$$\frac{\partial F_{LR}}{\partial U_R} = \frac{1}{2}\frac{\partial F_R}{\partial U_R} - sign(S_L)\frac{S_L}{2}\frac{\partial U_L^*}{\partial U_R} - sign(S_M)\frac{S_M}{2}(\frac{\partial (U_R^* - U_L^*)}{\partial U_R}) - sign(S_R)\frac{S_R}{2}(1 - \frac{\partial U_R^*}{\partial U_R}) \tag{145}$$

Where :

$$U_L^* = \frac{1}{S_M - S_L}[F_L - S_L U_L - (0, P^*, S_M.P^*)^T] \tag{146}$$

$$U_R^* = \frac{1}{S_M - S_R}[F_R - S_R U_R - (0, P^*, S_M.P^*)^T] \tag{147}$$

$$\frac{\partial U_L^*}{\partial U_L} = \frac{(\frac{\partial F_L}{\partial U_L} - S_L - \frac{\partial}{\partial U_L}(0, P^*, S_M.P^*)^T)(S_M - S_L) - (F_L - S_L U_L - (0, P^*, S_M.P^*)^T)\frac{\partial S_M}{\partial U_L}}{(S_M - S_L)^2} \tag{148}$$

$$\frac{\partial U_L^*}{\partial U_R} = \frac{-\frac{\partial}{\partial U_L}((0, P^*, S_M.P^*)^T)(S_M - S_L) - (F_L - S_R U_L - (0, P^*, S_M.P^*)^T)\frac{\partial S_M}{\partial U_R}}{(S_M - S_L)^2} \tag{149}$$

$$\frac{\partial U_R^*}{\partial U_L} = \frac{-\frac{\partial}{\partial U_L}((0, P^*, S_M.P^*)^T)(S_M - S_R) - (F_R - S_R U_R - (0, P^*, S_M.P^*)^T)\frac{\partial S_M}{\partial U_L}}{(S_M - S_R)^2} \tag{150}$$

$$\frac{\partial U_R^*}{\partial U_R} = \frac{(\frac{\partial F_R}{\partial U_R} - S_R - \frac{\partial}{\partial U_R}(0, P^*, S_M.P^*)^T)(S_M - S_R) - (F_R - S_R U_R - (0, P^*, S_M.P^*)^T)\frac{\partial S_M}{\partial U_R}}{(S_M - S_R)^2} \tag{151}$$

Using Relations 140, 141, and $P_L^* = P_R^* = P^*$, two expressions for P^* are obtained:

$$P^* = F_L(2) - S_L U_L(2) - S_M(F_L(1) - S_L U_L(1)) \tag{152}$$

and

$$P^* = F_R(2) - S_R U_R(2) - S_M(F_R(1) - S_R U_R(1)) \tag{153}$$

Nevertheless, in order to have a more precise derivative, the following average expression is used for P^*:

$$P^* = \frac{F_R(2) - S_R U_R(2) - S_M(F_R(1) - S_R U_R(1)) + F_L(2) - S_L U_L(2) - S_M(F_L(1) - S_L U_L(1))}{2} \tag{154}$$

$$\frac{\partial P^*}{\partial U_L} = \frac{1}{2}\left[\frac{\partial F_L(2)}{\partial U_L} - S_L(0,1,0)^T - S_M\left(\frac{\partial F_L(1)}{\partial U_L} - S_L(1,0,0)^T\right) - (F_L(1) - S_L U_L(1))\frac{\partial S_M}{\partial U_L}\right] \tag{155}$$

$$\frac{\partial P^*}{\partial U_R} = \frac{1}{2}\left[\frac{\partial F_R(2)}{\partial U_R} - S_R(0,1,0)^T - S_M\left(\frac{\partial F_R(1)}{\partial U_R} - S_R(1,0,0)^T\right) - (F_R - S_R U_R)\frac{\partial S_M}{\partial U_R}\right] \tag{156}$$

$$S_M = \frac{S_R U_R(2) - S_L U_L(2) - (F_R(2) - F_L(2))}{S_R U_R(1) - S_L U_L(1) - (F_R(1) - F_L(1))} \tag{157}$$

$$\begin{aligned}\frac{\partial S_M}{\partial U_L} =& \frac{(\frac{\partial F_L(2)}{\partial U_L} - S_L\frac{\partial U_L(2)}{\partial U_L})(S_R U_R(1) - S_L U_L(1) - (F_R(1) - F_L(1)))}{(S_R U_R(1) - S_L U_L(1) - (F_R(1) - F_L(1)))^2} \\ &- \frac{(S_R U_R(2) - S_L U_L(2) - (F_R(2) - F_L(2)))(\frac{\partial F_L(1)}{\partial U_L} - S_L\frac{\partial U_L(1)}{\partial U_L})}{(S_R U_R(1) - S_L U_L(1) - (F_R(1) - F_L(1)))^2}\end{aligned} \tag{158}$$

$$\begin{aligned}\frac{\partial S_M}{\partial U_R} =& \frac{(S_R\frac{\partial U_R(2)}{\partial U_R} - \frac{\partial F_R(2)}{\partial U_R})(S_R U_R(1) - S_L U_L(1) - (F_R(1) - F_L(1)))}{(S_R U_R(1) - S_L U_L(1) - (F_R(1) - F_L(1)))^2} \\ &- \frac{(S_R U_R(2) - S_L U_L(2) - (F_R(2) - F_L(2)))(S_R\frac{\partial U_R(1)}{\partial U_R} - \frac{\partial F_R(1)}{\partial U_R})}{(S_R U_R(1) - S_L U_L(1) - (F_R(1) - F_L(1)))^2}\end{aligned} \tag{159}$$

These various derivatives require the knowledge of $\frac{\partial F_L}{\partial U_L}$ and $\frac{\partial F_R}{\partial U_R}$. They correspond to the Jacobian matrix of the Euler equations. In the single phase flow situation the pressure is given by the Stiffened-Gas equation of state [14], [25], [27] :

$$P = (\gamma - 1)\rho e - \gamma P_\infty$$

With this EOS, the Jacobian matrix reads (with $m = \rho u$ and $\xi = \rho E$) :

$$J = \begin{Bmatrix} 0 & 1 & 0 \\ \frac{m^2}{2\rho^2}(\gamma - 3) & (3-\gamma)\frac{m}{\rho} & \gamma\text{ - }1 \\ -\frac{\gamma m \xi}{\rho^2} + (\gamma - 1)\frac{m^3}{\rho^3} + \frac{m\gamma P_\infty}{\rho^2} & \gamma\frac{\xi}{\rho} - \frac{3}{2}\frac{m^2(\gamma-1)}{\rho^2} - \frac{\gamma P_\infty}{\rho} & \frac{\gamma m}{\rho} \end{Bmatrix}$$

Slight changes have to be done with the two phase flow model. They are detailed in the next appendix.

Appendix C - High order extension

MUSCL type reconstruction [44] is considered. Variables extrapolation from the cell center i and the cell boundary (ij) is achieved by the following relation:

$$f_{ij} = f_i + \Phi_i \overrightarrow{\nabla f}_i \bullet \overrightarrow{r_{ij}} \tag{160}$$

where $\overrightarrow{r_{ij}}$ is the vector connecting the cell center and the intercell face, $\overrightarrow{\nabla f}_i$ is the approximate gradient of variable f in cell i and Φ_i the limiter ($\Phi_i \leq 1$).

The function gradient is approximated by weighted least squares.
The gradient $\overrightarrow{\nabla f}$ is defined by:

$$df = \overrightarrow{\nabla f} \bullet \overrightarrow{dM} \tag{161}$$

With the following notations:

$$\overrightarrow{\nabla f} = \begin{pmatrix} a \\ b \\ c \end{pmatrix}$$

To determine the gradient components a, b and c, the neighbouring cells are considered. Relation (161) expressed between the various cell faces and the cell center provides N relations ($N = 4$ for tetrahedron):

$$f_j - f_i = a(x_j - x_i) + b(y_j - y_i) + c(z_j - z_i), j = 1, N \tag{162}$$

where f_j represents the value of the f function at the center of the j cell while x_j, y_j and z_j represent the coordinates of the center of the j cell.

Thus, the following overdetermined system is obtained:

$$M\Delta f = D \tag{163}$$

where M is a (Nx3) matrix whereas Δf and D are size 3 vectors. To make benefit of this overdetermination, System (163) is multiplied by the M transpose.

$$M^T M\Delta f = M^T D \tag{164}$$

A new system is thus obtained,

$$M^*\Delta f = D^*, \tag{165}$$

with,

$$M^* = \begin{bmatrix} \sum \Delta x_{i,j}^2 & \sum \Delta x_{i,j}\Delta y_{i,j} & \sum \Delta x_{i,j}\Delta z_{i,j} \\ \sum \Delta x_{i,j}\Delta y_{i,j} & \sum \Delta y_{i,j}^2 & \sum \Delta y_{i,j}\Delta z_{i,j} \\ \sum \Delta x_{i,j}\Delta z_{i,j} & \sum \Delta y_{i,j}\Delta z_{i,j} & \sum \Delta z_{i,j}^2 \end{bmatrix}$$

$$D^* = \begin{bmatrix} \sum \Delta x_{i,j}\Delta f_{i,j} \\ \sum \Delta y_{i,j}\Delta f_{i,j} \\ \sum \Delta z_{i,j}\Delta f_{i,j} \end{bmatrix}$$

where :
$\Delta x_{i,j} = x_j - x_i$
$\Delta y_{i,j} = y_j - y_i$
$\Delta z_{i,j} = z_j - z_i$
$\Delta f_{i,j} = f_j - f_i$

However, the matrix M^* determinant can become very small if some cells are very close. To overcome this situation, one way to proceed is to use weights. A very simple weighting procedure has been proposed in [23]. It consists in modifying System (165) as follows:

$$M^* = \begin{bmatrix} \sum w_{i,j}^2 \Delta x_{i,j}^2 & \sum w_{i,j}^2 \Delta x_{i,j} \Delta y_{i,j} & \sum w_{i,j}^2 \Delta x_{i,j} \Delta z_{i,j} \\ \sum w_{i,j}^2 \Delta x_{i,j} \Delta y_{i,j} & \sum w_{i,j}^2 \Delta y_{i,j}^2 & \sum w_{i,j}^2 \Delta y_{i,j} \Delta z_{i,j} \\ \sum w_{i,j}^2 \Delta x_{i,j} \Delta z_{i,j} & \sum w_{i,j}^2 \Delta y_{i,j} \Delta z_{i,j} & \sum w_{i,j}^2 \Delta z_{i,j}^2 \end{bmatrix}$$

$$D^* = \begin{bmatrix} \sum w_{i,j}^2 \Delta x_{i,j} \Delta f_{i,j} \\ \sum w_{i,j}^2 \Delta y_{i,j} \Delta f_{i,j} \\ \sum w_{i,j}^2 \Delta z_{i,j} \Delta f_{i,j} \end{bmatrix}$$

where $w_{i,j} = \dfrac{1}{\sqrt{\Delta x_{i,j}^2 + \Delta y_{i,j}^2 + \Delta z_{i,j}^2}}$.
This correction guarantees that the determinant of M^* is $O(1)$.

The last step in the higher order extension method deals with gradients limitation. The Barth and Jespersen [4] method is adopted. For each i cell, the gradient limitation of a f function works as follows:

Computations of the minimum and maximum of f such as,

$$f_{max} = max(f_i, f_{j|j \in Vo(i)}),$$

and

$$f_{min} = min(f_i, f_{j|j \in Vo(i)}).$$

Then, for each neighbour j of i, the two following steps are achieved.
The function $\Phi_{i,j}$ used in Equation (160) is determined as:
-First compute $\Phi_{i,j}$ for each cell boundary as:

$$\Phi_{i,j} = \begin{cases} min(1, \dfrac{f_{min} - f_i}{f_{ij} - f_i}), & if\ (f_{i,j} - f_i) > 0 \\ min(1, \dfrac{f_{max} - f_i}{f_{ij} - f_i}), & if\ (f_{i,j} - f_i) < 0 \\ 1 & if\ (f_{i,j} - f_i) = 0 \end{cases}$$

- Then, Φ_i is computed as:

$$\Phi_i = min(\Phi_{i,j|j \in v(i)}), \tag{166}$$

Appendix D -Mixture pressure derivatives

The mixture pressure for the two-phase non-equilibrium model reads:

$$P = \sum_{k=1}^{N} \alpha_k p_k$$

where N is the number of fluids.
With the help of the EOS (2) it becomes:

$$P = \sum_{k=1}^{N} \left[(\gamma_k - 1)\alpha_k \rho_k e_k - \alpha_k \gamma_k P_{\infty,k} \right] \tag{167}$$

The volume fraction of fluid N is determined from the saturation constraint :

$$\alpha_N = 1 - \sum_{k=1}^{N-1} \alpha_k$$

Thus, equation (167) becomes:

$$P = \sum_{k=1}^{N} (\gamma_k - 1)\alpha_k \rho_k e_k + \sum_{k=1}^{N-1} \alpha_k (\gamma_N P_{\infty,N} - \gamma_k P_{\infty,k}) - \gamma_N P_{\infty,N} \tag{168}$$

With the following derivatives:

$$\frac{\partial P}{\partial \alpha_k \rho_k e_k} = \gamma_k - 1$$

$$\frac{\partial P}{\partial \alpha_k} = (\gamma_N P_{\infty,N} - \gamma_k P_{\infty,k})$$

Appendix E -Implicit schemes for non-conservative equations of the two-phase flow model

Volume fraction implicit scheme

In one-dimension, the volume fraction equation of System (5) reads:

$$\frac{\partial \alpha_1}{\partial t} + u \frac{\partial \alpha_1}{\partial x} = 0$$

The Godunov method for advection equations reads:

$$\alpha_{1,i}^{n+1} = \alpha_{1,i}^{n} + \frac{\Delta t}{\Delta x} \left[\left(\alpha_{1,i-1}^{n} - \alpha_i^n \right) S_{M,i-\frac{1}{2}}^{+} - \left(\alpha_{1,i+1}^{n} - \alpha_i^n \right) S_{M,i+\frac{1}{2}}^{-} \right]$$

Where :
S_M represents the contact wave speed and
$S_{M,i-\frac{1}{2}}^{+} = \frac{1}{2} \left(1 + sign(S_{M,i-\frac{1}{2}}) \right) S_{M,i-\frac{1}{2}}$,

$S_{M,i+\frac{1}{2}}^{-} = \frac{1}{2} \left(1 - sign(S_{M,i+\frac{1}{2}}) \right) S_{M,i+\frac{1}{2}}$.

Let's denote by:

$$\begin{cases} f_{Li}^n = \left(\alpha_{1,i-1}^n - \alpha_i^n\right) S_{M,i-\frac{1}{2}}^+ = \left(1 + sign(S_{M,i-\frac{1}{2}})\right)\left(\alpha_{1,i-1}^n - \alpha_i^n\right)\dfrac{S_{M,i-\frac{1}{2}}}{2} \\ f_{Ri}^n = \left(\alpha_{1,i+1}^n - \alpha_i^n\right) S_{M,i+\frac{1}{2}}^- = \left(1 - sign(S_{M,i+\frac{1}{2}})\right)\left(\alpha_{1,i+1}^n - \alpha_i^n\right)\dfrac{S_{M,i+\frac{1}{2}}}{2} \end{cases}$$

Thus, the implicit scheme for the volume fraction equation reads:

$$\alpha_{1,i}^{n+1} = \alpha_{1,i}^n - \frac{\Delta t}{\Delta x}\left[f_{Ri}^{n+1} - f_{Li}^{n+1}\right] \tag{169}$$

It is worth to mention that $f_{Ri} \neq f_{Li+1}$ as the equation is non-conservative.

Using the same development as previously (116 - 117), with $\delta\alpha_i = \alpha_{1,i}^{n+1} - \alpha_{1,i}^n$, the following scheme is obtained,

$$\left[I + \frac{\Delta t}{\Delta x}\left(\frac{\partial f_{Ri}}{\partial U_i} - \frac{\partial f_{Li}}{\partial U_i}\right)\right]\delta\alpha_i + \frac{\Delta t}{\Delta x}\frac{\partial f_{Ri}}{\partial U_{i+1}}\delta\alpha_{i+1} - \frac{\Delta t}{\Delta x}\frac{\partial f_{Ri}}{\partial U_{i-1}}\delta\alpha_{i-1} = -\frac{\Delta t}{\Delta x}\left(f_{Ri}^n - f_{Li}^n\right), \tag{170}$$

where U is represents the whole conservative variables vector.

Internal energies implicit scheme

In one-dimension, the internal energy equations read ($k = 1, 2$):

$$\frac{\partial \alpha_k \rho_k e_k}{\partial t} + \frac{\partial \alpha_k \rho_k e_k u}{\partial x} + \alpha_k p_k \frac{\partial u}{\partial x} = 0 \tag{171}$$

The explicit scheme used for this equation reads:

$$(\alpha\rho e)_k^{n+1} = (\alpha\rho e)_k^n - \frac{\Delta t}{\Delta x}\left((\alpha\rho e u)_{k,i+\frac{1}{2}}^{*,n} - (\alpha\rho e u)_{k,i-\frac{1}{2}}^{*,n} + (\alpha p)_{k,i}^n\left(u_{i+\frac{1}{2}}^{*,n} - u_{i-\frac{1}{2}}^{*,n}\right)\right) \tag{172}$$

where the product $(\alpha_k p_k)_i^n$ is assumed constant during the time step and the superscript " $*$ " denotes the Riemann problem solution state .

Thus, the implicit scheme for the internal energy equations read:

$$(\alpha\rho e)_k^{n+1} = (\alpha\rho e)_k^n - \frac{\Delta t}{\Delta x}\left((\alpha\rho e u)_{k,i+\frac{1}{2}}^{*,n+1} - (\alpha\rho e u)_{k,i-\frac{1}{2}}^{*,n+1} + (\alpha p)_{k,i}^{n+1}\left(u_{i+\frac{1}{2}}^{*,n+1} - u_{i-\frac{1}{2}}^{*,n+1}\right)\right) \tag{173}$$

Using the same development as previously (116 - 117) with $F_{ek} = (\alpha\rho e u)_k$ and $\delta(\alpha\rho e)_{k,o} = (\alpha\rho e)_{k,i}^{n+1} - (\alpha\rho e)_{k,i}^n$, the following scheme is obtained:

$$\begin{aligned} &\left[I + \frac{\Delta t}{\Delta x}\left(\frac{\partial F_{ek,i+\frac{1}{2}}^n}{\partial U_i} - \frac{\partial F_{ek,i-\frac{1}{2}}^n}{\partial U_i} + (\alpha p)_{k,i}^n\left[\frac{\partial u_{i+\frac{1}{2}}^*}{\partial U_i} - \frac{\partial u_{i-\frac{1}{2}}^*}{\partial U_i}\right] + (u_{i+\frac{1}{2}}^* - u_{i-\frac{1}{2}}^*)\frac{\partial (\alpha p)_{k,i}^n}{\partial U_i}\right)\right]\delta(\alpha\rho e)_{k,i} \\ &+ \frac{\Delta t}{\Delta x}\left[\frac{\partial F_{ek,i+\frac{1}{2}}}{\partial U_{i+1}} + (\alpha p)_{k,i}^n\frac{\partial u_{i+\frac{1}{2}}^*}{\partial U_{i+1}}\right]\delta(\alpha\rho e)_{k,i+1} - \frac{\Delta t}{\Delta x}\left[\frac{\partial F_{ek,i-\frac{1}{2}}}{\partial U_{i-1}} + (\alpha p)_{k,i}^n\frac{\partial u_{i-\frac{1}{2}}^*}{\partial U_{i-1}}\right]\delta(\alpha\rho e)_{k,i-1} \\ &= -\frac{\Delta t}{\Delta x}\left((\alpha\rho e u)_{k,i+\frac{1}{2}}^{*,n} - (\alpha\rho e u)_{k,i-\frac{1}{2}}^{*,n} + (\alpha p)_{k,i}^n\left(u_{i+\frac{1}{2}}^{*,n} - u_{i-\frac{1}{2}}^{*,n}\right)\right) \end{aligned} \tag{174}$$

Where $\frac{\partial F_{ek,i+\frac{1}{2}}}{\partial U_i}$, $\frac{\partial F_{ek,i+\frac{1}{2}}}{\partial U_{i+1}}$, $\frac{\partial F_{ek,i-\frac{1}{2}}}{\partial U_i}$ and $\frac{\partial F_{ek,i-\frac{1}{2}}}{\partial U_{i-1}}$ are calculated using the HLLC flux derivatives (Appendix 6).

Appendix F -Stiff thermodynamic relaxation

A two-phase liquid, vapor mixture in thermodynamic equilibrium is considered. Both phases are thus in pressure, temperature and Gibbs free energy equilibrium.
The thermodynamic equilibrium state is determined by considering the following algebraic system:

$$\begin{aligned} v &= \frac{1}{\rho} = Y_1 v_1 + Y_2 v_2 = cte = v_0 \\ e &= Y_1 e_1 + Y_2 e_2 = cte = e_0 \\ T_1 &= T_2 = T \\ p_1 &= p_2 = p \\ g_1 &= g_2 \end{aligned} \tag{175}$$

Where $Y_1 = \frac{\alpha_1 \rho_1}{\rho}$ and $Y_2 = \frac{\alpha_2 \rho_2}{\rho} = 1 - Y_1$ denote the mass fractions of both phases, which are not constant during the relaxation process.
The first two equations of this system come from the mass conservation and mixture total energy conservation, respectively. The last equation represents the Gibbs free energies equality ($g = h - Ts$).
The liquid and its vapor are denoted by the subscripts "1" and "2", respectively.
The specific volumes and the internal energies of each phase are given by the following expressions, based on the stiffened gas EOS (2):

$$v_k = \frac{(\gamma_k - 1) C_{v,k} T_k}{p_k + p_{\infty,k}} \tag{176}$$

$$e_k = C_{v,k} T_k \left(1 + \frac{(\gamma_k - 1) p_{\infty,k}}{p + p_{\infty,k}}\right) + q_k \tag{177}$$

Each parameter involved in the previous expressions ($\gamma_k, C_{v,k}, p_{\infty,k}, q_k$) is calculated in order to fit the liquid-vapor phase diagram, more precisely the corresponding saturation curves. Details regarding the EOS parameters determination are given in [27] and [39].
Denoting the final state by the superscript '*', the mass conservation constraint becomes:

$$v_0 = Y_1^* v_1^*(p^*) + Y_2^* v_2^*(p^*) = Y_1^* v_1^*(p^*) + (1 - Y_1^*) v_2^*(p^*), \tag{178}$$

with $v_1^*(p^*) = \frac{(\gamma_k - 1) C_{v,k} T^*(p^*)}{p^* + p_{\infty,k}}$.
Constraints of pressures, temperatures and Gibbs free energies equilibrium have been used in Relation (178). Indeed, the Gibbs free energies equality leads to a relationship between the pressure and the temperature:

$$T^*(p^*) = T_{sat}(p^*) \tag{179}$$

$v_1^*(p^*)$ and $v_2^*(p^*)$ represent the saturated specific volumes of both phases. A first relation linking the liquid mass fraction and the pressure is thus obtained:

$$Y_1^* = \frac{v_2^*(p^*) - v_0}{v_2^*(p^*) - v_1^*(p^*)} \tag{180}$$

Consider now the mixture total energy conservation:

$$e_0 = Y_1^* e_1^*(p^*) + Y_2^* e_2^*(p^*) = Y_1^* e_1^*(p^*) + (1 - Y_1^*) e_2^*(p^*) \tag{181}$$

with $e_k(p^*) = C_{v,k} T_k^*(p^*)(1 + \dfrac{(\gamma_k - 1)p_{\infty,k}}{p + p_{\infty,k}}) + q_k$
A second relation linking the liquid mass fraction and the pressure is thus obtained:

$$Y_1^* = \frac{e_0 - e_2^*(p^*)}{e_1^*(p^*) - e_2^*(p^*)} \tag{182}$$

This relation can be also expressed as a function of the specific enthalpies of each phase:

$$Y_1^* = \frac{h_2^*(p^*) - (e_0 - p^* v_0)}{h_2^*(p^*) - h_1^*(p^*)} \tag{183}$$

Where h_1 and h_2 are linked by $h_2^*(p^*) - h_1^*(p^*) = L_v(p^*)$, $L_v(p^*)$ representing the latent heat of vaporization, which is a function of the pressure.
From the previous mass fraction equations, a single function of the pressure is obtained:

$$\frac{h_2^*(p^*) - (e_0 - p^* v_0)}{h_2^*(p^*) - h_1^*(p^*)} - \frac{v_2^*(p^*) - v_0}{v_2^*(p^*) - v_1^*(p^*)} = 0 \tag{184}$$

Its solution is computed with the Newton method. Once the relaxed pressure is known, solution of this equation is determined, the remaining variables are easily determined with the preceding thermodynamic relations.

Contents

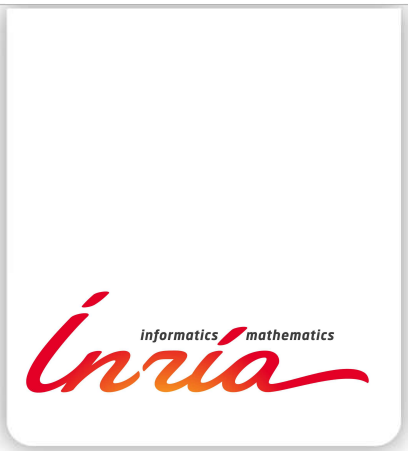

RESEARCH CENTRE
SOPHIA ANTIPOLIS – MÉDITERRANÉE

2004 route des Lucioles - BP 93
06902 Sophia Antipolis Cedex

Publisher
Inria
Domaine de Voluceau - Rocquencourt
BP 105 - 78153 Le Chesnay Cedex
inria.fr

ISSN 0249-6399